Hemicellulose Pyrolysis: Mechanism and Kinetics of Functionalized Xylopyranose

Leandro Ayarde-Henríquez,*[ab] Jacopo Lupi,[ab] and Stephen Dooley*[ab]

[a] School of Physics, Trinity College Dublin, Dublin, Ireland.
[b]Advanced Materials and BioEngineering Research Centre, Dublin, Ireland.

Abstract This work analyzes the thermochemical kinetic influence of the most prominent functionalizations of the β-D-xylopyranose motif, specifically 4-methoxy, 5-carboxyl, and 2-O-acetyl, regarding the pyrolytic depolymerization mechanism. The gas-phase potential energy surface of the initial unimolecular decomposition reactions is computed with M06-2X/6-311++G(d,p), following which energies are refined using the G4 and CBS-QB3 composite methods. Rate constants are computed using the transition state theory. The energies are integrated within the atomization method to assess for the first time the standard enthalpy of formation of β-D-xylopyranose, 4-methoxy-5-carboxy-β-D-xylopyranose, and 2-O-acetyl-β-D-xylopyranose: *-218.2*, *-263.1*, and *-300.0* kcal mol^{-1}, respectively. For all isomers, the activation enthalpies of ring-opening are considerably lower, *43.8-47.5* kcal mol^{-1}, than the ring-contraction and elimination processes, which show higher values ranging from *61.0-81.1* kcal mol^{-1}. The functional groups exert a notable influence, lowering the barrier of discrete elementary reactions by *1.9-8.3* kcal mol^{-1}, increasing thus the reaction rate constant by *0-4* orders of magnitude relative to unsubstituted species. Regardless of the functionalization, the ring-opening process always exhibits the highest reactivity characterized by a rate constant on the order of 10^{1} s^{-1}, significantly surpassing the values associated with ring-contraction and elimination, which fall in the range 10^{-4}-10^{-10} s^{-1}. Remarkably, these kinetics are contingent on the functionalization specificities and the relative orientation of reacting centers. A relatively simple chemical reactivity and bonding analysis partially support the elaborated thermokinetic approach. These insights hold significance as they imply that many alternative decomposition routes can be quickly, yet accurately, informed in forthcoming explorations of potential energy surfaces of diverse hemicellulose motifs under pyrolysis conditions.

Keywords: hemicellulose substituents effects, β-D-xylopyranose motif, Fast Pyrolysis technology, quantum chemical calculations, gas-phase thermo-kinetics

Introduction

In the contemporary global economic scenarios, predominant reliance persists on non-renewable energy resources, including coal, natural gas, and petroleum.[1,2] Recent assessments underscore that worldwide energy consumption has reached a staggering *412* exajoules per year (EJ/y),[1] displaying an upward trajectory for the past ten decades, barring any economic recessions. This escalating demand stresses the importance of identifying and harnessing alternative, sustainable fuel sources.[3] Fortunately, biomass emerges as a plentiful and renewable reservoir of sustainable carbon and hydrogen with the potential to provide up to *147* EJ in 2030.[1,2] Biomass broadly encompasses organic matter of plants and animals;[4,5] however, this term is usually restricted to the referring of botanical constituents. Plant biomass is a composite of diverse organic compounds, including lipids, sugars, and lignocellulose, the latter being the fundamental structural material of plants. The inherent complexity of lignocellulosic plant matter is illustrated through the relative proportions of its principal components: cellulose *40-60* %, hemicellulose *15-30* %, and lignin *10-25* %.[4,6] Cellulose, the most abundant saccharide on Earth,[7–10] is an ordered polymeric structure of glucose ($C_6H_{12}O_6$). Frequently, cellulose is represented in terms of its basic unit, namely, the degree of polymerization (*n*), highlighting its polysaccharide nature, i.e., $(C_6H_{10}O_5)_n$.[4,7] This renewable and biodegradable polymer has found wide-ranging applications across diverse food, textile, and plastics industries.[7] In contrast, hemicellulose is not a homopolysaccharide since it is formed by shorter chains, including mainly hexoses ($C_6H_{12}O_6$) and pentoses ($C_5H_{10}O_5$).[11,12] Conversely, lignin presents an amorphous polymeric structure of aromatic ether rings attached to a three-carbon propene tail,[13–15] as presented in Scheme 1.

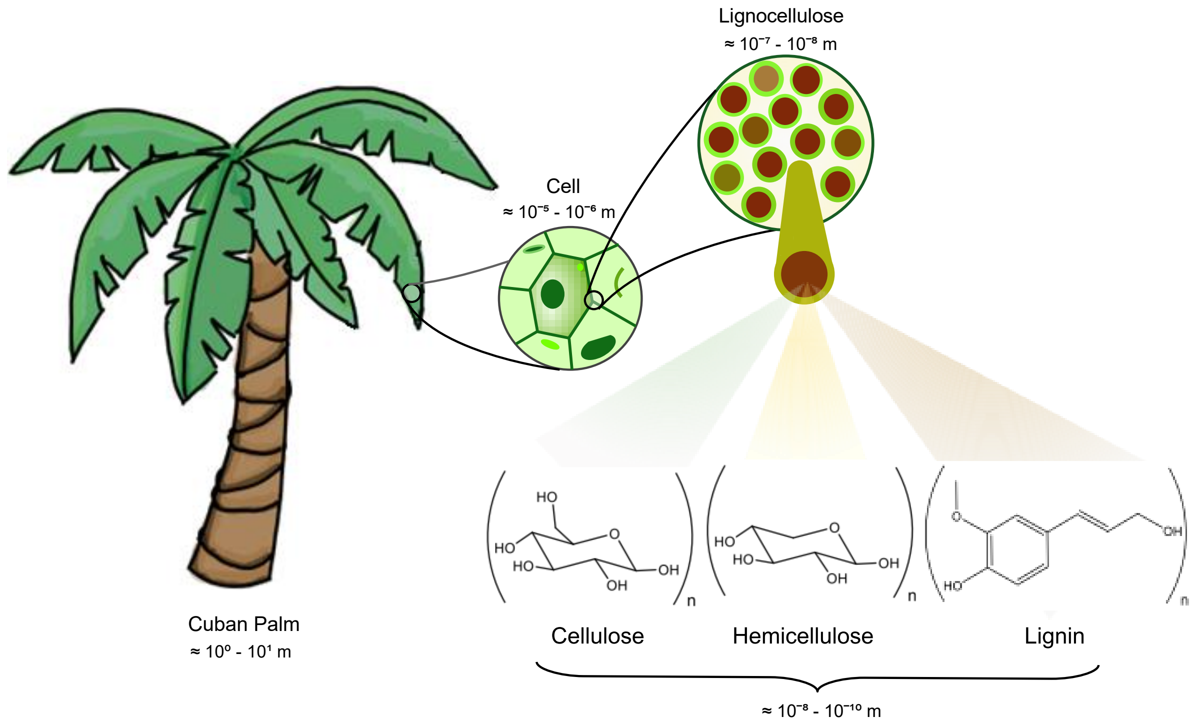

Scheme 1. Typical structural motifs for modeling the lignocellulose (biomass) building blocks: cellulose, hemicellulose, and lignin. This graphical representation stresses the scale and multiscale challenges, which limit the current understanding of the thermal conversion of biomass into valuable bioproducts.

The degradation of biomass to valuable chemicals and fuels by thermochemical processes, such as pyrolysis, gasification, hydrothermal liquefaction, and others, has captured the attention of the Industry, Government, and Academia.[3,4,6,16] Among all methods for degrading biomass, the so-called *Fast Pyrolysis* (FP) is considered the most attractive one.[1,17,18] This process is predicated on the thermal (≈ *400-600* °C, ≈ 10^3 °C/s) decomposition of biomass in an inert atmosphere, i.e., without oxygen,[1,19,20] and is a leading technology with regard to its technical and economic performance. In the context of the FP regime, it is essential to note that cellulose, hemicellulose, and lignin bio-oil yields exhibit characteristic values of approximately *70*, *60*, and *40* %, respectively. However, these values are notably sensitive to variations in temperature. This means that an increase or drop in the temperature will cause the system to deviate from these thermal operation conditions, impacting thus these yields.[21,22] Nowadays, the bio-oil produced falls short in terms of quality and cost-effectiveness compared to its petroleum-derived crude oil counterparts. This discrepancy is primarily attributed to several issues that must be surmounted before the commercial-scale utilization of bio-products can be achieved:[1,4,5,17,23] i. the chemical structural complexity and high variability of main biomass components, ii. challenges posed by the scale and multiscale problems, iii. the imperative development of effective technologies for characterizing biomass products, iv. the pressing need for accurate and *unified* kinetic models to predict the type and relative abundance of bioproducts. From our perspective, it is crucial to conduct *systematic* theoretical studies that account for the influence of both *metals* and *substituents* due to the current experimental limitations. This rigorous approach is pivotal for elucidating fundamental molecular physical knowledge underpinning the thermal depolymerization of biomass, facilitating the transition towards a bio-based and circular economy.

Recently, our research group has been actively immersed in developing a detailed kinetic model for the pyrolysis of hemicellulose and lignin. This model is poised for further refinement through the *Machine Learned Optimization of Chemical Kinetics* (MLOCK) coded algorithm.[24] MLOCK optimizes kinetic models to target data (e.g., experimental measurements) through the generation and evaluation of sets of solutions by simultaneous perturbation of Arrhenius parameters. Machine learning and data-analysis techniques are employed to direct the search algorithm towards the ideal set of solutions that results in a kinetic model of high fidelity to the optimization targets. Furthermore, it is well known that a minor content of minerals is present within the plant tissues in the form of cations, oxides, salts, phosphates, and sulfates.[1,17] This inorganic material encompasses a variety of minerals such as potassium (K), magnesium (Mg), sodium (Na), calcium (Ca), cobalt (Co), and copper (Cu).[1,17] It is essential to stress that these elements significantly impact the depolymerization processes, although the content is typically low, ranging from *2-25* % of the total mass.[1] It has been long reported[25–27] the presence of O-acetyl groups in hemicellulose of both hard and softwood. The precise positions of such groups, C2 and/or C3, were determined by combining nuclear magnetic resonance (NMR), thermogravimetric analysis (TGA), and chemical analysis. In addition, experimental investigations have successfully isolated 4-methoxy-5-carboxy-β-D-xylopyranose (henceforth referred to as 4-O-methyl-D-glucuronic acid) from different hemicellulose plant sources.[28,29] Thus, the current state-of-art of biomass treatment underscores the dynamic and highly promising landscape of contemporary studies, offering substantial opportunities for pioneering breakthroughs in the field.

It should be emphasized that considerable research efforts have been dedicated to investigating the thermal degradation mechanism of cellulose, leading to comparatively fewer studies on the other two primary biomass components.[27] In the existing literature, investigations addressing the depolymerization impact of substituents on the thermokinetic features of pyrolytic processes are scarce. Wang and co-workers[30] identified some products resulting from the breakage of O-acetyl groups and 4-O-methyl-D-glucuronic acid units from xylan by combining thermogravimetric and Fourier-transform infrared spectroscopy techniques. Huang et al.,[31] proposed some reaction pathways for products of 2-O-acetyl-β-D-xylopyranose (hereafter termed 2-O-acetyl-xylose) upon pyrolysis. However, to the best of our knowledge, there is a *conspicuous absence of prior studies concerning the systematic assessment of the influence of functional groups on hemicellulose depolymerization*, even though some studies show that the amount of O-acetyl groups could significantly impact the product yields and condition bio-oils' acidity.[18,32–34] Consequently, this work aims to discuss to what extent functional groups affect the pyrolytic degradation of the hemicellulose motif, β-D-xylopyranose (hereafter referred to as xylose), from both thermodynamical and kinetic viewpoints. Subsequent systematic works will address other biomass components (e.g., lignin), the organic-inorganic interaction, and the transferring of all these insights to our kinetic model.

Computational Methods

Considering the amount of excellent bibliographical sources available, we here will briefly outline the basic aspects of the methods used in this study. Geometry optimizations were performed at the M06-2X/6-311++G(d,p) level of theory using the Gaussian 16 code.[35] This global hybrid functional is parametrized for non-metal elements and has been recommended for investigations encompassing main-group thermochemistry and kinetics.[36] For all cases, the intrinsic reaction coordinate (IRC)[37] was followed to ensure the transition state (TS) connects the correct reactant and product(s). As a standard procedure, the stationary points on the IRC were characterized as minima (i.e., reactants, intermediates, and products) and first-order saddle points (TSs) based on the vibrational frequency signs. The adequacy of our single-reference-based methodology was assessed via the T_1 diagnostic[38] for key species along the pathways. The static correlation is insignificant for the investigated systems, meaning multireference methods are not required since $T_1 < 0.02$. See the Electronic Supplementary Information (ESI) for further details.

Conformational analysis for critical species (e.g., minima and TSs) along the IRC was conducted using the CREST program.[39] This software combines semiempirical tight-binding methods with meta-dynamics to generate conformers thermodynamic ensembles within a relatively narrow energy window of *4.87* kcal mol^{-1}. This set of structures was further optimized at the M06-2X/6-311++G(d,p) level and compared with those observed in scattering experiments to ensure the study of the correct enantiomer.

In order to obtain accurate thermochemistry values at both absolute zero and *298* K, composite model chemistry methods such as the complete basis set (CBS)[40,41] and Gaussian-4 (G4)[42] were employed. In these approaches, geometry optimizations and frequency calculations are performed using relatively simple and cost-effective methods, adding higher levels of theory in a stepwise manner.

The temperature dependence of thermodynamical properties such as the Gibbs free energy (ΔG) and heat capacities (Cp and Cv) was conducted under the rigid-rotor harmonic oscillator (RRHO) approximation using the Shermo 2.3.5 suite.[43] This is a pretty flexible code that allows the explicit consideration of scaling factors of vibrational frequencies for several quantities, including the zero-point vibrational energy (ZPE), for determining thermochemical values and automatically treating the low frequencies via Grimme's[44] entropy interpolation between harmonic and free-rotor approximations on an ideal gas behavior assumption. It is worth mentioning that Lu and Chen[43] showed that applying quasi-RRHO (QRRHO) schemes for treating hindered internal rotors in relatively flexible molecules moderately impacts entropy (*S*). Based on harmonic approximation, the *Cp* is computed as follows:

$$Cp(T) = R\left[1 + \sum_i \left(\frac{h\upsilon_i}{k_B T}\right)^2 \frac{e^{-h\upsilon_i/(k_B T)}}{\left(1 - e^{-h\upsilon_i/(k_B T)}\right)^2}\right] \tag{1}$$

As anticipated, the symbols $k_B, h,$ and R represent pivotal physical metrics: Boltzmann's constant, Planck's constant, and the universal constant of the ideal gas, respectively. The vibrational frequency of mode i is indicated by υ_i, whereas T is the absolute temperature. Considering the substantial flexibility inherent to carbohydrates, the impact of many thermally accessible conformations is methodically integrated through a conventional statistical Boltzmann weighting procedure to obtain accurate thermodynamical properties.

The standard enthalpy of formation, ΔH_f^0 at *298* K, of chemical species was computed using Rogers et al.'s methodology.[45] This procedure combines experimental[46,47] and atoms code-generated thermochemistry data to accurately derive the values of ΔH_f^0 by using the reaction enthalpy, ΔH_r^0, as a proxy. Let us exemplify this algorithm by considering the formation of one molecule of water from its constituents (atoms) in their standard state:

$$\Delta H_f^0(\mathrm{H_2O}) = \sum_{atoms} \Delta H_f^0 + \Delta H_r^0 = \left[2\Delta H_f^0(\mathrm{H}) + \Delta H_f^0(\mathrm{O})\right] + \left[H(\mathrm{H_2O}) - 2H(\mathrm{H}) - H(\mathrm{O})\right] \tag{2}$$

In equation (2), the first squared bracket comprises the experiment-derived quantities reported in the Active Thermochemical Tables (ATcT).[46,47] In contrast, the second one encapsulates the parameters to be computed using sophisticated suites such as Gaussian.[35]

The reaction kinetics analysis was performed within the (conventional) transition state theory (TST), considering the reaction path degeneracy and the Eckart tunneling effects using the KiSThelP 2021 package of codes.[48] This software facilitates the exploration of kinetic features of the potential energy surface (PES) for both uni and bimolecular reactions under different temperature and pressure setups through a wide range of TST levels, including also vibrational scaling factors. In this context, the rate constant, $k(T)$, of each elementary step is determined through the following expression:

$$k(T) = \chi(T)\frac{n^{\ddagger}\sigma}{n\sigma^{\ddagger}}\frac{k_B T}{h}\frac{Z^{\ddagger}}{N_A Z}e^{-V^{\ddagger}/(k_B T)} \tag{3}$$

where N_A represents Avogadro's number. Quantum mechanical effects (e.g., tunneling) on the reaction coordinate motion are integrated via the coefficient of transmission, $\chi(T)$. The terms n and $n^{\ddagger}$ represent the number of chiral isomers of the reactant(s) and the transition state, respectively, while σ and $\sigma^{\ddagger}$ are the corresponding rotational symmetry numbers of these states. Moreover, the difference in the potential energy, $V^{\ddagger}$, between the transition state and reactant(s) does not include zero-point contributions as these are considered in their corresponding partition function, $Z^{\ddagger}$ and Z, respectively. KiSThelP2021 allows for describing the temperature dependency of the rate constant by fitting the data to a two-parameter conventional Arrhenius equation:

$$k(T) = Ae^{-E_a/(RT)} \tag{3}$$

As expected, A is the pre-exponent or frequency factor, and E_a stands for the activation energy.

The chemical reactivity assessment was conducted by calculating the electronic chemical potential, μ,[49] and Fukui's functions (f^+, f^-, and f^0).[50] The parameter μ measures the global tendency of electrons to escape from a ground-state system.[49,51] Conversely, the f indices describe the local response of the molecule to nucleophilic (f^+), electrophilic (f^-), and neutral/radical (f^0) attacks.[50,52–54] Additionally, the bonding analysis was performed using the electron localization function (ELF).[55,56] ELF is frequently interpreted as a local measure of electrons' kinetic energy excess due to Pauli's exclusion principle;[57,58] thus, high values of this function (> *0.5*) correspond to spatial position with high electron localization.[59,60] The nullity condition applied to the ELF gradient yields a partition of the molecular space into basins of attractors, empirically associated with Lewis' bonding elements, including valence bonds, lone pairs, and atomic cores.[61,62] The numerical computation underlying the chemical reactivity and bonding analysis was carried out using the Multiwfn packages,[63] a standard tool for performing electronic wavefunction analysis.

Results and Discussion

Thermochemical Insights

Various structural motifs have been used to investigate the depolymerization of hemicellulose under different experimental setups.[5] Lu et al.[64] extensively studied the pyrolytic mechanism of xylose, 1,4-β-D-xylobiose, and xylan by combining experimental and computational methodologies. They employed a gas-chromatograph (GC) coupled to a mass spectrometer (MS) to analyze and identify the products generated upon pyrolysis of these hemicellulose motifs. Next, a detailed reaction network comprising about *50* processes was proposed to elucidate the depolymerization of xylose, including three elemental initial steps: ring-opening, ring-contraction, and elimination. Consequently, this system is chosen as a prototypical structure for modeling hemicellulose in this study. Our goal is to assess the impact of substituents through the use of functionalized species such as 2-O-acetyl-xylose and 4-O-methyl-D-glucuronic acid undergoing the same initial reactions, as illustrated in Scheme 2. This strategic approach provides a systematic basis for hierarchically ordering subsequent steps along the decomposition channels. The ring-opening leads to an acyclic product via the bond scission between the pyran-ring oxygen (O) and the carbon at position 1 (C1). Conversely, furfural (FF) and furfural-like (FFL) compounds result from the ring-contraction process through both carbon-carbon (CC) and carbon-oxygen (CO) breakages. At last, reacting species undergo eliminations at positions 1, 2, 3, and 4 upon the bond cleavage of carbons at these sites and the oxygen atom of hydroxyl, methoxy, and O-acetyl groups. This process leads to the formation of anhydroxylopyranose (AXP), anhydroxylopyranose-like (AXPL), acetic acid (AA), and methanol. The simplest system yields AXP, whereas the other three form upon the initial pyrolytic reactions of substituted reactants. The ring-contraction and elimination entail the transfer of the proton situated at neighboring positions to the cleaving CO bond, which emphasizes the intricacies of such elementary steps.

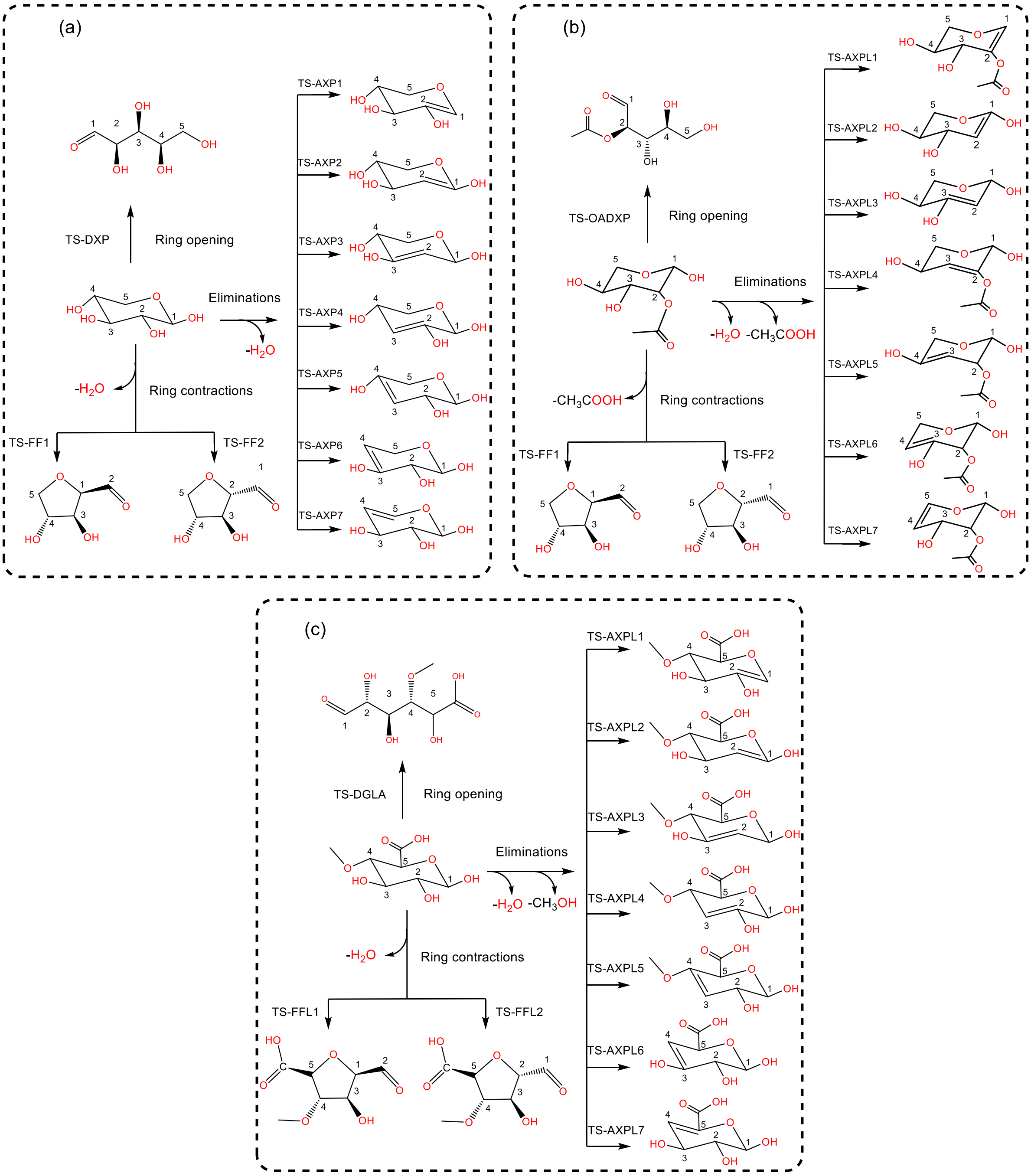

Scheme 2. Lewis-like structures illustrating a simple kinetic model comprising key initial depolymerization reactions[64] of xylose (Panel a). Functionalized chemical species 2-O-acetyl-xylose (Panel b) and 4-O-methyl-D-glucuronic acid (Panel c) undergo the same reactions to systematically assess the influence of substituents. For all systems, the ring-opening process comprises the C1-O bond cleavage leading to an acyclic form, the ring-contraction involves the transformation of the pyran ring to a five-membered ring, and anhydroxylopyranose forms through elimination.

Table 1 shows the relative enthalpy of activation, $\Delta H^{\ddagger}$, at both *0* and *298* K of substituted and unsubstituted species concerning the ring opening/contraction and elimination processes at three levels of theory. It is worth noting that the transition states (TSs) of reactions comprising the conversion from the pyran to FF configuration, TS-FFL1 and TS-FFL2, failed to converge for 2-O-acetyl-xylose, showing the inherent complexities in modeling such processes. The arithmetic average of $\Delta H^{\ddagger}$ was computed using the G4 and CBS-QB3 data to compensate for possible underestimation and overestimation effects. Interestingly, the description provided by the highest level (G4) and the mean differs substantially. This evidence the fundamental differences in the state-of-the-art levels of theory integrated within G4 and CBS-QB3, particularly in their capabilities to describe correlation effects. The electronic energy accuracy provided by CCSD(T) and QCSD(T) plays a significant role in this discrepancy. The arithmetic mean shows a significant difference of $\Delta \overline{H}^{\ddagger} > 5$ kcal mol^{-1} for the ring-opening undergone by the double-functionalized system relative to the simplest system. Contrary to the results obtained with G4. This Gaussian-family method reveals that the presence of the O-acetyl group at C2 significantly lowers the activation enthalpy (≈ *8* kcal mol^{-1}) of processes directly involving the substituent, specifically TS-AXPL2 and TS-AXPL3. Similarly, by comparing xylose and 4-O-methyl-D-glucuronic acid results, it is evident the relatively high difference in $\Delta H^{\ddagger}$ for the elimination at C4 (undergone via TS-AXPL7), which comprises the methoxy group. This is expected for TSs involving such a group; however, we found other dehydrations characterized by $\Delta H^{\ddagger} > 5$ kcal mol^{-1}, exemplified by the reactions associated with TS-AXPL2 and TS-AXPL4. As indicated by the G4 composite method, it is pertinent to conduct an in-depth examination of the s*teric* and *regioselectivity* effects to elucidate the underlying mechanisms influencing the apparent favorable direction in processes comprising proton transfers.

Table 1. Activation enthalpies, $\Delta H^{\ddagger}$, in kcal mol^{-1} at both *0* and *298* K regarding the initial elementary reactions undergone by xylose, 2-O-acetyl-xylose, and 4-O-methyl-D-glucuronic acid at different levels of theory.

	T = 0 K				**T = 298 K**			
Species	$\Delta H^{\ddagger}_{DFT}$	$\Delta H^{\ddagger}_{CBS}$	$\Delta H^{\ddagger}_{G4}$	$\overline{\Delta H}^{\ddagger}$	$\Delta H^{\ddagger}_{DFT}$	$\Delta H^{\ddagger}_{CBS}$	$\Delta H^{\ddagger}_{G4}$	$\overline{\Delta H}^{\ddagger}$
DXP	49.68	38.19	45.55	41.87	45.54	37.30	45.54	41.42
FF1	76.21	-	71.41	71.41	72.84	-	71.47	71.47
FF2	70.25	56.68	65.07	60.88	70.25	56.68	65.09	60.88
AXP1	75.55	62.03	69.11	65.57	70.57	61.64	69.65	65.65
AXP2	87.20	73.70	80.73	77.22	82.00	73.27	81.08	77.18
AXP3	79.73	66.27	73.49	69.88	74.55	65.69	73.76	69.73
AXP4	81.45	67.78	74.86	71.32	76.08	67.40	75.20	71.30
AXP5	80.08	66.41	74.05	70.23	74.78	65.96	74.39	70.18
AXP6	81.68	67.01	74.38	70.70	76.07	66.46	74.85	70.66
AXP7	77.19	64.26	71.49	67.88	71.81	63.48	71.56	67.52
OADXP	45.56	43.99	43.91	43.95	42.65	43.89	43.79	43.84
FFL1	-	-	-	-	-	-	-	-
FFL2	-	-	-	-	-	-	-	-
AXPL1	70.71	68.04	67.72	67.88	66.07	68.33	67.94	68.14
AXPL2	79.36	73.76	73.28	73.52	74.39	74.32	73.80	74.06
AXPL3	70.94	65.25	65.14	65.20	65.77	65.55	65.43	65.49
AXPL4	75.77	72.43	71.94	72.19	70.84	72.72	72.19	72.46
AXPL5	77.76	71.49	71.32	71.41	72.57	71.63	71.43	71.53
AXPL6	76.33	73.10	72.38	72.74	71.17	73.58	72.79	73.19
AXPL7	75.25	70.38	69.78	70.80	69.60	70.49	69.87	70.18
DGLA	51.87	47.77	47.66	47.72	47.36	47.76	47.47	47.62
FFL1	82.85	-	-	-	79.21	-	-	-
FFL2	67.35	60.91	61.01	60.96	64.66	60.94	61.03	60.98
AXPL1	75.64	70.19	68.79	69.49	70.49	70.62	69.27	69.95
AXPL2	85.70	75.67	75.29	75.48	81.37	75.53	75.10	75.32
AXPL3	80.77	74.82	74.29	74.56	75.62	75.19	74.60	74.90
AXPL4	73.24	69.40	68.89	69.15	68.71	69.38	68.78	69.08
AXPL5	78.65	73.87	73.51	73.69	73.68	74.23	73.84	74.04
AXPL6	79.67	72.23	72.28	72.26	74.73	72.85	72.92	72.89
AXPL7	66.35	63.95	63.53	63.74	62.58	64.08	63.70	63.89

DFT stands for M06-2X/6-311++G(d,p).

CBS stands for CBS-QB3.

The arithmetic mean of $\overline{\Delta H}^{\ddagger}$ was computed using both the G4 and CBS-QB3 data.

The standard enthalpy of formation, $\Delta H_f^0(298\,\mathrm{K})$, of atoms and molecules is a critical thermodynamical parameter in the comprehensive analysis of gas-phase combustion processes employing detailed kinetic models. This metric characterizes the energy change when one mole of a substance is produced under standard conditions from its pure elements in their standard states. The determination of this energetic parameter encompasses a spectrum of methodologies, including isodesmotic[65,66] and connectivity-based hierarchy (CBH)[44,67] schemes. In our study, we determined $\Delta H_f^0(298\,\mathrm{K})$ for reactants and products resulting from the initial elementary steps through the methodology outlined by Rogers and collaborators.[45] This procedure combines experimental[46,47] and atomization thermochemistry data generated via computational algorithms to calculate ΔH_f^0 by considering the reaction enthalpy of various isodesmic[68] and homodesmotic[68] reactions. Therefore, the reaction enthalpy serves as a proxy for the enthalpies of formation as it is involved in the conservation equations, facilitating computing the heat release at discrete intervals of time. The atomization approach, relying on the precision of the methods to describe the electronic structure rather than leveraging error cancellations, was adopted to assess the influence of functional groups on the relative stability of the investigated compounds. Its simplicity and reasonable accuracy guided this selection.[45,69] The evaluation of water, methanol, and acetic acid (AA) in the gas phase reveals discrepancies not surpassing *0.50* kcal mol^{-1} between the experimental and computed values when corrections for spin-orbit couplings (SOC)[70,71] of carbon and oxygen atoms are integrated *a posteriori* within the atomization scheme to fine-tune ΔH_f^0, as presented in Table 2. Notably, the absolute error decreases by *0.16*, *0.20*, and *0.50* kcal mol^{-1} for the corresponding species when such a correction is considered; these values are presented in parentheses in Table 2. This trend indicates the potential significant influence of SOC effects on the accuracy of the predicted ΔH_f^0, particularly for moieties characterized by a relatively high molecular weight.

Table 2. Standard enthalpy of formation, $\Delta H_f^0(298\,\mathrm{K})$, in kcal mol^{-1} of reactants and products resulting from ring-opening, ring-contraction, and eliminations. The values within parentheses exclude spin-orbit coupling corrections.

Species	ΔH_f^0	Formula	Species	ΔH_f^0	Formula	Species	ΔH_f^0	Formula
Xylose	-218.15 (-216.91)	C5H10O5	2-O-acetyl-xylose	-263.08 (-261.51)	C7H12O6	4OMGLA	-299.99 (-298.26)	C7H12O7
DXP	-209.65 (-208.41)	C5H10O5	OADXP	-253.62 (-252.05)	C7H12O6	DGLA	-291.27 (-289.54)	C7H12O7
FF1	-145.27 (-144.20)	C5H8O4	FFL1	-145.28 (-144.20)	C5H8O4	FFL1	-229.11 (-227.55)	C7H10O6
FF2	-145.96 (-144.88)	C5H8O4	FFL2	-146.06 (-144.99)	C5H8O4	FFL2	-230.49 (-228.92)	C7H10O6
AXP1	-145.78 (-144.71)	C5H8O4	AXPL1	-189.18 (-187.77)	C7H10O5	AXPL1	-226.61 (-225.05)	C6H8O6
AXP2	-152.76 (-151.69)	C5H8O4	AXPL2	-152.77 (-151.69)	C7H10O5	AXPL2	-232.26 (-230.69)	C6H8O6
AXP3	-150.87 (-149.80)	C5H8O4	AXPL3	-148.49 (-147.41)	C7H10O5	AXPL3	-233.14 (-231.57)	C7H10O6
AXP4	-149.52 (-148.44)	C5H8O4	AXPL4	-190.48 (-189.08)	C7H10O5	AXPL4	-228.63 (-227.07)	C7H10O6
AXP5	-152.56 (-151.49)	C5H8O4	AXPL5	-199.94 (-198.54)	C5H8O4	AXPL5	-233.80 (-232.23)	C7H10O6
AXP6	-150.47 (-149.40)	C5H8O4	AXPL6	-200.34 (-198.93)	C5H8O4	AXPL6	-238.97 (-237.49)	C7H10O6
AXP7	-149.79 (-148.72)	C5H8O4	AXPL7	-202.59 (-201.19)	C7H10O5	AXPL7	-237.89 (-236.41)	C7H10O6
H_2O	-57.46[1] (-57.30)	H2O	AA	-102.95[2] (-102.46)	C2H4O2	Methanol	-48.12[3] (-47.87)	CH4O

[1] The experimental value is equal to (*-57.80 ± 0.02*) kcal mol^{-1}. See Ruscic et al.[46]

[2] The experimental value is equal to (*-103.41 ± 0.27*) kcal mol^{-1}. See Ruscic et al.[46]

[3] The experimental value is equal to (*-47.80 ± 0.15*) kcal mol^{-1}. See Ruscic et al.[46]

The heat capacity of materials is a fundamental metric in thermodynamics, aiding in the precise calculation of thermal requirements and optimal processing temperatures. Furthermore, it serves as a discriminative parameter in distinguishing between two distinct polymeric composites based on their thermal characteristics.[72] On the other hand, the entropy (*S*) of gases is a quantitative measure that encapsulates the statistical ensemble nature of a gas system, delineating the extent of randomness or disorder within the ensemble and not corresponding to a macroscopic property. The values of *S* are greater when the vectors characterizing the individual motions of the gas molecules exhibit heightened disorder, as opposed to scenarios where all molecules demonstrate high organization, moving uniformly in a singular direction at uniform velocities.[73] In this context, the heat capacities at constant volume (*Cv*) and pressure (*Cp)*, as well as the entropy, were computed assuming that reactants and products resulting from the initial depolymerization reactions exist in the gas phase and can be modeled as ideal gases. The low values of *Cp* increase with rising temperatures for all species. As anticipated, the pyran-ring structures have lower values than their corresponding acyclic form since the latter molecular configuration is less rigid, which favors the contribution of additional vibrational degrees of freedom. The influence of functional groups is evident since larger structures, in terms of the number of atoms, are characterized by higher *Cp*. For instance, at *200* K and *1.0* atm, the heat capacity of 2-O-acetyl-xylose and 4-O-methyl-D-gluguronic acid are *22.9* and *27.7* % higher, respectively, than that of xylose. Such percentages slightly decrease as the absolute temperature increases.

At a temperature of *381.20* K and under *1.0* atm of pressure, calorimetric experiments conducted by McCullough and co-workers[74] give a value of *0.0088* kcal mol^{-1} K^{-1} for the water vapor, characterized by an expected uncertainty not greater than ±*0.2* %. Notably, our calculations yield *0.0082* kcal mol^{-1} K^{-1} at *400* K, showing a close agreement with the experimental data. However, they applied statistical procedures to compensate for deviations driven by gas imperfections since the apparent heat capacity decreased as the temperature increased. This observation contrasts with our computational findings, which do not display such a trend, as evidenced in Table 3.

In a separate study, Stull and collaborators[75] compiled a thermochemical dataset spanning over several decades, comprising *741* pure organic compounds in the gas phase. Such a collection of experimental values was previously obtained by combining thermal and spectroscopic direct measurements. For water, the computed *Cp* in the range of *300* to *1 000* K deviates by *1.6* % at most from the corresponding experimental value. Furthermore, this remarkable trend is also observed for acetic acid (AA) and methanol; see Table 3.

Goldberg and collaborators[76] performed rigorous combustion calorimetric measurements on the crystalline alpha anomer of xylose, specifically α-D-xylopyranose. Their investigation covered a wide temperature range from *1.9* to *305* K and used an isoperibol static bomb calorimeter. They reported an experimental value equal to *Cp* = (*0.04254* ± *0.00180*) kcal mol^{-1} K^{-1} at *298.15* K, which deviates *3.21* % from other measures obtained through similar experimental setups.[77,78] Surprisingly, the *Cp* provided by Goldberg closely approximates the computed one for the beta isomer in the gas phase at *300* K. In contrast, the *Cp* = (*0.06716* ± *0.002*) kcal mol^{-1} K^{-1} of the α configuration in the aqueous phase at *303* K found by Kawaizumi et al.[78] is about *60* % higher. Additional details concerning computed values of *Cv* and *S* for all species in the gas phase can be found in the ESI.

Table 3. Heat capacity, *Cp*, in kcal mol^{-1} K^{-1} at different temperatures of chemical species involved in the initial elementary reactions: ring-opening, ring-contraction, and elimination.

Species	**T/K 200**	**300**	**400**	**500**	**600**	**700**	**800**	**900**	**1 000**
Xylose	0.02935	0.04030	0.05075	0.05989	0.06740	0.07349	0.07851	0.08270	0.08626
DXP	0.03244	0.04277	0.05263	0.06126	0.06839	0.07421	0.07904	0.08310	0.08657
FF1	0.02567	0.03435	0.04308	0.05081	0.05721	0.06245	0.06677	0.07038	0.07345
FF2	0.02591	0.03446	0.04312	0.05082	0.05722	0.06245	0.06678	0.07040	0.07346
AXP1	0.02544	0.03494	0.04385	0.05153	0.05780	0.06287	0.06704	0.07053	0.07348
AXP2	0.02539	0.03492	0.04389	0.05160	0.05787	0.06294	0.06709	0.07057	0.07351
AXP3	0.02481	0.03445	0.04352	0.05130	0.05763	0.06276	0.06696	0.07047	0.07345
AXP4	0.02507	0.03464	0.04364	0.05137	0.05768	0.06280	0.06699	0.07050	0.07346
AXP5	0.02495	0.03463	0.04365	0.05139	0.05770	0.06281	0.06701	0.07051	0.07348
AXP6	0.02531	0.03481	0.04376	0.05146	0.05776	0.06286	0.06705	0.07054	0.07351
AXP7	0.02526	0.03480	0.04385	0.05161	0.05792	0.06300	0.06716	0.07063	0.07357
H_2O	0.00795	0.00800 (0.00803)	0.00816 (0.00819)	0.00839 (0.00842)	0.00864 (0.00868)	0.00890 (0.00895)	0.00916 (0.00925)	0.00943 (0.00955)	0.00969 (0.00985)
2-O-acetyl-xylose	0.03806	0.05136	0.06441	0.07588	0.08534	0.09305	0.09942	0.10475	0.10927
OADXP	0.04135	0.05416	0.06649	0.07735	0.08639	0.09383	0.10001	0.10522	0.10966
FFL1	0.02556	0.03428	0.04303	0.05078	0.05719	0.06243	0.06676	0.07038	0.07344
FFL2	0.02578	0.03441	0.04314	0.05088	0.05727	0.06250	0.06681	0.07042	0.07348
AXPL1	0.03416	0.04604	0.05748	0.06746	0.07569	0.08241	0.08796	0.09261	0.09654
AXPL2	0.02537	0.03491	0.04389	0.05159	0.05787	0.06294	0.06710	0.07057	0.07351
AXPL3	0.02469	0.03442	0.04358	0.05139	0.05772	0.06283	0.06701	0.07050	0.07345
AXPL4	0.03437	0.04607	0.05747	0.06745	0.07568	0.08242	0.08797	0.09262	0.09656
AXPL5	0.03388	0.04578	0.05732	0.06736	0.07562	0.08235	0.08791	0.09256	0.09650
AXPL6	0.03345	0.04548	0.05713	0.06723	0.07552	0.08229	0.08786	0.09252	0.09646
AXPL7	0.03257	0.04490	0.05683	0.06711	0.07549	0.08228	0.08786	0.09251	0.09644
AA	0.01268	0.01625 (0.01597)	0.01977 (0.01952)	0.02286 (0.02260)	0.02546 (0.02515)	0.02763 (0.02735)	0.02946 (0.02908)	0.03103 (0.03060)	0.03239 (0.03199)
4OMGLA	0.04061	0.05469	0.06822	0.08008	0.08986	0.09783	0.10439	0.10987	0.11450
DGLA	0.04207	0.05623	0.06953	0.08107	0.09059	0.09837	0.10480	0.11019	0.11477
FFL1	0.03624	0.04838	0.06033	0.07085	0.07957	0.08671	0.09259	0.09750	0.10165
FFL2	0.03648	0.04849	0.06037	0.07086	0.07958	0.08671	0.09260	0.09752	0.10167
AXPL1	0.03629	0.04916	0.06124	0.07167	0.08023	0.08719	0.09291	0.09768	0.10171
AXPL2	0.03645	0.04930	0.06141	0.07185	0.08039	0.08733	0.09303	0.09778	0.10179
AXPL3	0.03556	0.04855	0.06081	0.07137	0.08001	0.08703	0.09279	0.09760	0.10165
AXPL4	0.03662	0.04928	0.06130	0.07172	0.08028	0.08724	0.09297	0.09774	0.10177
AXPL5	0.03580	0.04882	0.06102	0.07153	0.08014	0.08713	0.09286	0.09765	0.10168
AXPL6	0.03234	0.04440	0.05525	0.06432	0.07159	0.07740	0.08212	0.08601	0.08929
AXPL7	0.03308	0.04491	0.05559	0.06456	0.07177	0.07754	0.08221	0.08608	0.08934
Methanol	0.00946	0.01079 (0.01052)	0.01270 (0.01229)	0.01470 (0.01422)	0.01653 (0.01602)	0.01815 (0.01762)	0.01956 (0.01904)	0.02081 (0.02029)	0.02191 (0.02138)

The experiment-derived values of water, acetic acid, and methanol are provided in round brackets. See Stull et al.[75]

Techno-economic analysis (TEA) is a methodological approach aiming to evaluate the viability of an emerging technology prior to its commercial deployment.[79–83] TEA has been extensively applied to assess processes in several industrial sectors, including chemicals, renewable energy, transportation fuel, carbon utilization technologies, desalination technology, and biogas.[81,84] To effectively achieve this ambitious goal, TEA strategically integrates the design, simulation, and assessment of the cash flow of the process. This framework yields essential economic metrics that facilitate comprehensive investment decision-making, considering both technological and economic perspectives.[80–83]

Not surprisingly, the quality of biofuels is inherently contingent upon their physical (e.g., bulk density and gross calorific value) chemical composition (e.g., total content of carbon, hydron, and oxygen).[85,86] The set of products resulting from the initial steps comprises both low- and high-molecular-weight structures. Notably, methanol and acetic acid (AA), which correspond to the former subset, form from elimination reactions involving the methoxy and O-acetyl functional groups, respectively. Alcohols generally manifest the highest combustion efficiency owing to their relatively elevated oxygen content,[86] thereby substantiating their intrinsic value as a fuel source. Furthermore, Wang and collaborators[30] have shown that O-acetyl groups could be dissociated at relatively moderate temperatures ranging from *473.15* to *573.15* K, resulting in a significant increase in the acidity of bio-oils. This stresses the necessity for thoroughly evaluating the influence of substituted species to carry out an exhaustive TEA of biofuels, as real-world lignocellulosic is a complex organic matrix, bearing indeed the functional groups here investigated, as illustrated in Figure 1.

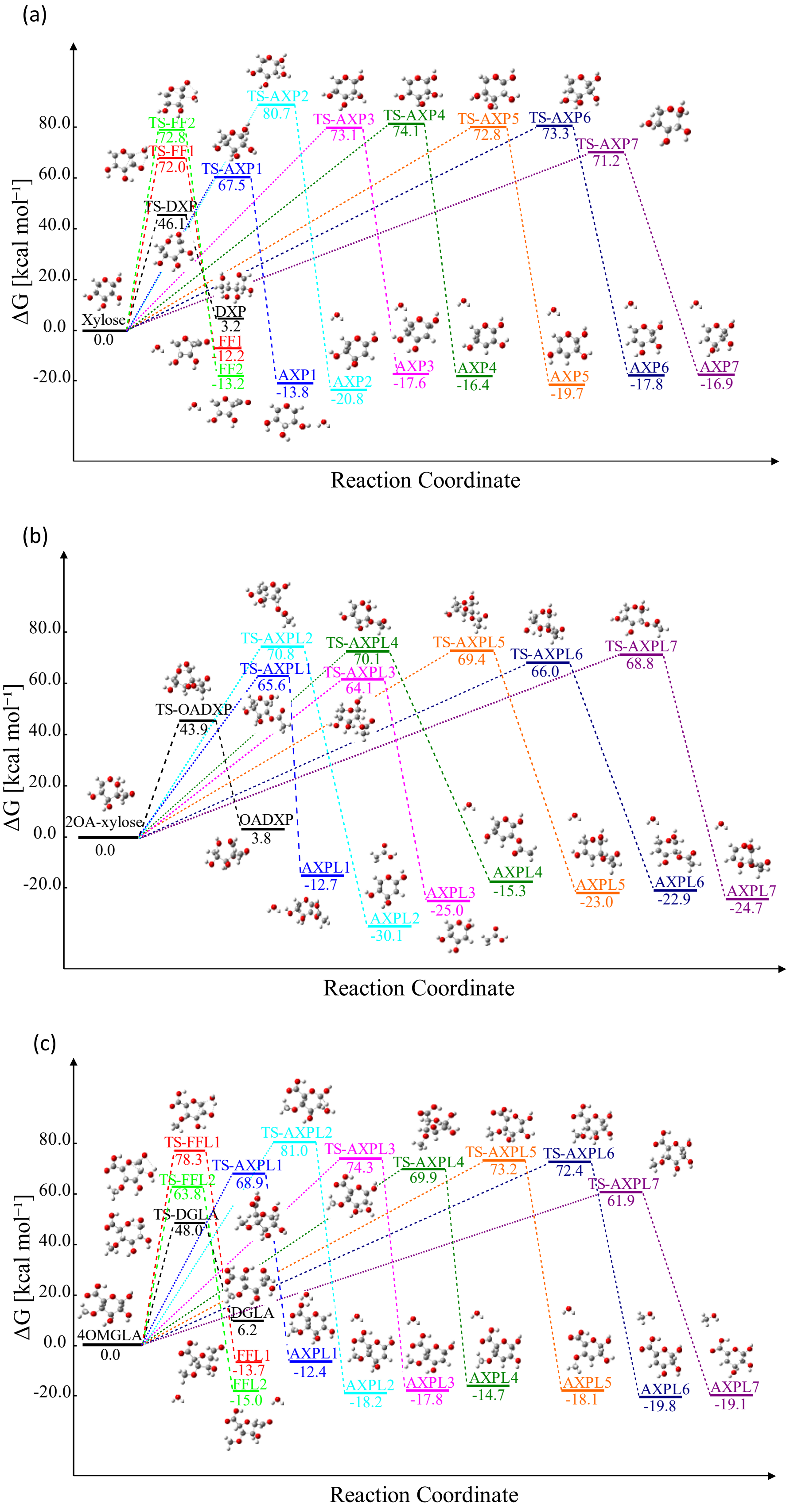

Figure 1. Gibbs free energy at *773.15* K of key structures featuring the thermal depolymerization of hemicellulose structural motifs: xylose (Panel a), 2-O-acetyl-xylose (Panel b), and 4-O-methyl-D-glucuronic acid (Panel c). DXP, OADXP, and DGLA denote the acyclic fragments of the ring-opening of xylose, 2-O-acetyl-xylose, and 4-O-methyl-D-glucuronic acid, respectively. FF*j* and FFL*j* (*j=1,2*) correspond to the products of the ring-contraction, and AXP*i* and AXPL*i* (*i=1,2.,…,7*) represent the moieties resulting from eliminations undergone by xylose and functionalized species, respectively. The molecular configurations are color-coded: carbons in grey, oxygens in red, and hydrogens in white.

Kinetic Findings

The analysis of the Gibbs free energy, *ΔG*, reveals distinct thermodynamic behaviors among the species studied. For xylose, the onset of favorable ring-opening steps is observed only at temperatures exceeding *800* K. In contrast, *ΔG > 0* for both substituted systems in the temperature interval of *400* to *1 000* K indicates the thermodynamic non-favorability of this reaction. All the other processes proceed in the forward direction across this temperature range for the simplest reactant and 4-O-methyl-D-glucuronic acid. However, the elimination process leading to the AXPL1 product is unfavorable at the lowest temperature for the single-substituted system, as shown in Table 4. It is worth noting that *400* K falls completely outside the FP domain.

Table 4. Free energies, *ΔG*, in kcal mol^{-1} of reactants and products resulting from the ring-opening, ring-contraction, and elimination initial steps.

Reaction **T/K**	**400**	**500**	**600**	**700**	**800**	**900**	**1000**
Xylose	0	0	0	0	0	0	0
D-xylose	2.01	1.49	0.99	0.49	0.01	-0.45	-0.90
FF1 + H_2O	-1.72	-5.80	-9.84	-13.84	-17.79	-21.70	-25.56
FF2 + H_2O	-2.71	-6.82	-10.89	-14.91	-18.89	-22.82	-26.70
AXP1 + H_2O	-0.87	-4.83	-8.79	-12.74	-16.66	-20.56	-24.43
AXP2 + H_2O	-7.83	-11.84	-15.85	-19.86	-23.83	-27.79	-31.71
AXP3 + H_2O	-5.72	-9.58	-13.44	-17.27	-21.08	-24.85	-28.60
AXP4 + H_2O	-4.26	-8.16	-12.05	-15.93	-19.77	-23.59	-27.38
AXP5 + H_2O	-6.67	-10.60	-14.53	-18.44	-22.33	-26.20	-30.03
AXP6 + H_2O	-5.13	-9.06	-12.99	-16.89	-20.77	-24.63	-28.45
AXP7 + H_2O	-3.05	-7.05	-11.04	-15.01	-18.96	-22.88	-26.77
2-O-acetyl-xylose	0	0	0	0	0	0	0
OADXP	4.32	3.73	3.13	2.53	1.94	1.34	0.75
FFL1 + CH_3COOH	-3.89	-8.82	-13.74	-18.65	-23.55	-28.42	-33.29
FFL2 + CH_3COOH	-5.06	-9.99	-14.92	-19.84	-24.74	-29.62	-34.49
AXPL1 + H_2O	1.43	-2.58	-6.60	-10.61	-14.59	-18.56	-22.50
AXPL2 + CH_3COOH	-15.11	-19.92	-24.75	-29.60	-34.44	-39.28	-44.11
AXPL3 + CH_3COOH	-11.49	-16.21	-20.94	-25.67	-30.38	-35.08	-39.76
AXPL4 + H_2O	-0.73	-4.87	-9.01	-13.14	-17.25	-21.34	-25.40
AXPL5 + H_2O	-9.44	-13.42	-17.40	-21.36	-25.30	-29.22	-33.10
AXPL6 + H_2O	-9.64	-13.56	-17.47	-21.38	-25.27	-29.12	-32.95
AXPL7 + H_2O	-10.00	-13.84	-17.68	-21.52	-25.35	-29.15	-32.93
4OMGLA	0	0	0	0	0	0	0
DGLA	2.19	1.98	1.77	1.57	1.36	1.17	0.97
FFL1 + H_2O	-4.34	-8.41	-12.46	-16.46	-20.43	-24.35	-28.24
FFL2 + H_2O	-5.81	-9.92	-14.00	-18.04	-22.04	-26.00	-29.92
AXPL1 + H_2O	-0.05	-4.02	-7.99	-11.95	-15.89	-19.80	-23.68
AXPL2 + H_2O	-5.23	-9.30	-13.37	-17.44	-21.49	-25.52	-29.51
AXPL3 + H_2O	-6.76	-10.72	-14.68	-18.62	-22.54	-26.43	-30.29
AXPL4 + H_2O	-2.52	-6.62	-10.71	-14.78	-18.83	-22.86	-26.85
AXPL5 + H_2O	-5.58	-9.58	-13.58	-17.58	-21.56	-25.52	-29.45
AXPL6 + CH_3OH	-7.34	-11.88	-16.41	-20.93	-25.44	-29.92	-34.38
AXPL7 + CH_3OH	-6.92	-11.58	-16.25	-20.91	-25.55	-30.17	-34.77

From a kinetic perspective, the ring-opening reaction exhibits the highest rate for all species; see Figure 2, Panels a-c. However, the presence of substituents induces some qualitative and quantitative changes. Among all processes, the ring-opening shows the least sensitivity to temperature changes, evidenced by the lowest tilt of its rate line. The functional groups close the competing gap as the temperature increases, which is more evident for the moiety characterized by the highest number of substituent groups, i.e., 4-O-methyl-D-glucuronic acid. For xylose, the water elimination at C1 undergone through TS-AXP1, the dehydration at C4 associated with TS-AXP7, and the ring-contraction linked to TS-FF2 are the second, third, and fourth fastest processes, respectively; in contrast, this ranking shifts to TS-AXPL7, TS-FFL2, and TS-AXPL1 for the double-substituted species. In the case of 2-O-acetyl-xylose, one of the reactions involving the substituent (TS-AXPL3) will still lie within the three fastest depolymerization events, even assuming that both elementary reactions associated with TS-FFL1 and TS-FFL2 could be faster. Surprisingly, the other elimination involving the functional group (TS-AXPL2) is the lowest reaction. This underscores and further supports our previous thermodynamic findings regarding the radically different behavior between processes comprising the same functional group, see Figure 2, Panel d. Therefore, the kinetic analysis also raises the need to include the directionality of proton transfers and the steric effects. Regardless of the relatively high vibrational frequency of TSs associated with ring-opening and eliminations, the Eckart tunneling effects are extremely weak because temperatures characterizing the FP regimen greatly surpass the cross-over temperature (≈ *92-458* K). Consequently, the tunneling is shallow and points out that rate constants can be computed using the classical rate theory.[87,88]

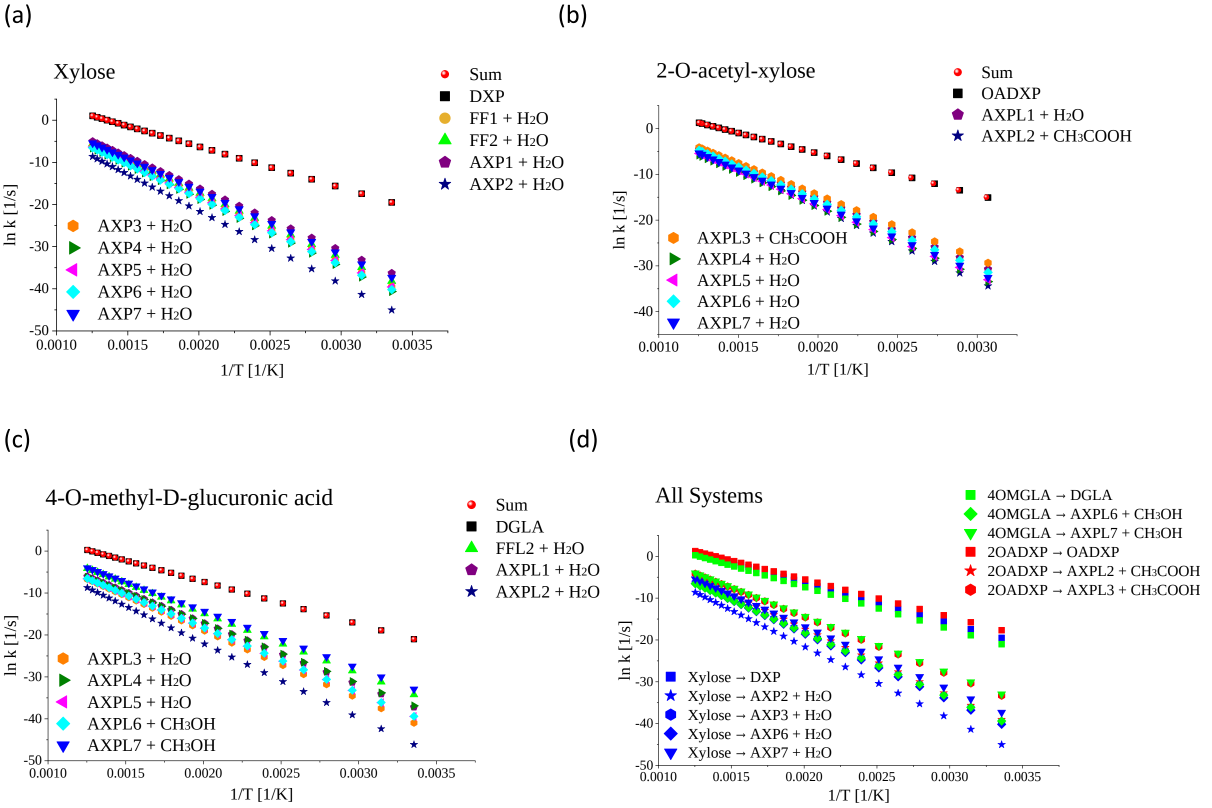

Figure 2. Rate constants dependence on the inverse of the absolute temperature. Panel a shows the rate lines of xylose's initial steps: ring-opening (Xylose ⟶ DXP), ring-contractions (Xylose ⟶ FF1 + H_2O and Xylose ⟶ FF2 + H_2O), and eliminations (Xylose ⟶ AXP*i* + H_2O, *i = 1,…,7*). Panel b illustrates the rate lines of 2-O-acetyl-xylose's initial reactions: ring-opening (2-O-acetyl-xylose ⟶ OADXP) and eliminations (2-O-acetyl-xylose ⟶ AXPL*j* + H_2O, *j = 1, 4,…,7* and 2-O-acetyl-xylose ⟶ AXPL*k* + CH_3COOH, *k = 2,3*). Panel c depicts the rate lines of 4-O-methyl-D-glucuronic acid's initial processes: ring-opening (4OMGLA ⟶ DGLA), ring-contraction (4OMGLA ⟶ FFL2 + H_2O), and eliminations (4OMGLA ⟶ AXPL*l* + H_2O, *l = 1,…,5* and 4OMGLA ⟶ AXPL*m* + CH_3COOH, *m = 6,7*). Panel d stresses that functional groups influence the processes involving them mostly; however, the extent of this impact strongly depends on the side of the proton transfer. This is illustrated via color-coded symbols: xylose in red, 2-O-acetyl-xylose in blue, and 4-O-methyl-D-glucuronic acid in green.

Table 5 presents a detailed overview of the fitted value of the frequency factor, *A*, and activation energy, E_a, for each elementary reaction undergone by the three chemical species under investigation. In the case of the simplest system, the highest values of *A* correspond to the ring-contractions FF1 and FF2. In contrast, for the O-acetyl functionalized species, the *A* maximum value corresponds to one of the elementary reactions involving the substituent, i.e., TS-AXPL2. As expected, the same trend is observed in the case of the double-functionalized system. These findings show the consistency between the thermodynamic and kinetic findings concerning that substituents indeed exert a catalytic-like effect in both functionalized species. However, the extent of this effect is contingent upon the relative spatial arrangement of the reacting centers, particularly the specific side of the proton attack. More importantly, while discernible, the influence of functional groups is insufficient to substantially bridge the competition gap between the ring-opening reaction and the other elementary steps.

Table 5. Arrhenius fit parameters for the initial reactions of substituted and unsubstituted systems over the interval [*400*, *1 000*] K. The rate constant is computed at *773.15* K.

Elementary Reaction	A [s^{-1}]	E_a [kcal mol^{-1}]	k [s^{-1}]	k/k_{sum} [%]
Xylose ⟶ DXP	1.68×10^{13}	44.68	4.11	100.00
Xylose ⟶ FF1	8.79×10^{13}	72.71	2.63×10^{-7}	6.40×10^{-6}
Xylose ⟶ FF2	7.44×10^{13}	64.62	4.28×10^{-5}	1.04×10^{-3}
Xylose ⟶ AXP1	3.79×10^{13}	68.06	2.33×10^{-6}	5.70×10^{-5}
Xylose ⟶ AXP2	1.17×10^{13}	79.31	4.80×10^{-10}	1.17×10^{-8}
Xylose ⟶ AXP3	3.17×10^{13}	72.39	1.17×10^{-7}	2.85×10^{-6}
Xylose ⟶ AXP4	5.06×10^{13}	74.17	5.86×10^{-8}	1.42×10^{-6}
Xylose ⟶ AXP5	2.46×10^{13}	72.26	9.86×10^{-8}	2.40×10^{-6}
Xylose ⟶ AXP6	3.26×10^{13}	73.28	6.74×10^{-8}	1.64×10^{-6}
Xylose ⟶ AXP7	1.69×10^{13}	70.12	2.72×10^{-7}	6.62×10^{-6}
2-O-acetyl-xylose ⟶ OADXP	3.23×10^{12}	41.87	4.90	100.00
2-O-acetyl-xylose ⟶ FF1	-	-	-	-
2-O-acetyl-xylose ⟶ FF2	-	-	-	-
2-O-acetyl-xylose ⟶ AXPL1	3.95×10^{13}	66.27	7.77×10^{-6}	1.58×10^{-4}
2-O-acetyl-xylose ⟶ AXPL2	5.03×10^{14}	73.31	1.02×10^{-6}	2.08×10^{-5}
2-O-acetyl-xylose ⟶ AXPL3	1.84×10^{13}	63.64	2.00×10^{-5}	4.08×10^{-4}
2-O-acetyl-xylose ⟶ AXPL4	3.94×10^{13}	69.62	8.78×10^{-7}	1.79×10^{-5}
2-O-acetyl-xylose ⟶ AXPL5	8.61×10^{13}	70.33	1.21×10^{-6}	2.47×10^{-5}
2-O-acetyl-xylose ⟶ AXPL6	2.43×10^{13}	68.66	1.01×10^{-6}	2.06×10^{-5}
2-O-acetyl-xylose ⟶ AXPL7	3.97×10^{13}	69.62	8.85×10^{-7}	1.81×10^{-5}
4-O-methyl-D-glucuronic acid ⟶ DGLA	8.39×10^{12}	46.41	6.66×10^{-1}	99.95
4-O-methyl-D-glucuronic acid ⟶ FFL1	-	-	-	-
4-O-methyl-D-glucuronic acid ⟶ FFL2	1.23×10^{13}	62.20	3.41×10^{-5}	5.12×10^{-3}
4-O-methyl-D-gluguronic acid ⟶ AXPL1	3.38×10^{12}	67.94	2.25×10^{-7}	3.38×10^{-5}
4-O-methyl-D-glucuronic acid ⟶ AXPL2	1.77×10^{12}	76.56	4.34×10^{-10}	6.51×10^{-8}
4-O-methyl-D-glucuronic acid ⟶ AXPL3	5.39×10^{13}	74.64	4.60×10^{-8}	6.90×10^{-6}
4-O-methyl-D-glucuronic acid ⟶ AXPL4	1.19×10^{12}	66.99	1.47×10^{-7}	2.21×10^{-5}
4-O-methyl-D-glucuronic acid ⟶ AXPL5	8.93×10^{13}	71.50	5.87×10^{-7}	8.81×10^{-5}
4-O-methyl-D-glucuronic acid ⟶ AXPL6	1.04×10^{13}	71.53	6.70×10^{-8}	1.01×10^{-5}
4-O-methyl-D-glucuronic acid ⟶ AXPL7	1.80×10^{14}	63.04	2.89×10^{-4}	4.34×10^{-2}

Chemical Reactivity and Bonding Analysis

Macro thermodynamical variables, such as heat capacity, derive their origins from micro-level features. The kinetic of particles (e.g., vibrational and translational velocities) serves as the physical basis of an intensive state variable we call temperature. This emphasizes the significance of delving into the molecular physics underpinning the thermal conversion of biomass into a wide variety of bioproducts as a critical step before integrating sustainable materials into practical applications. The valence-shell electron-pair repulsion theory (VSEPR)[89] leverages electrostatic considerations to accurately predict the molecular geometry of a wide variety of systems ranging from organic to inorganic compounds. Given the fundamental relationship between geometry, properties, and applications, our approach involves computing the electron population of each reactant as an initial step. This calculation constitutes a building block for establishing the intricate link between macro-level thermodynamics and micro-level molecular interactions through chemical bonding analysis of ELF. Such a methodical approach has been broadly applied in both the solid-state and gas-phase to deepen our understanding across different covalent bonding situations,[90,91] proton transfer reactions,[92] C-H bonds activation,[93] phase transition of the 14 group elements,[94] cycloadditions,[95–103] hemiaminals formation,[104,105] photoreactions,[103,106–111] arynes production,[112] computing local and global properties of solids,[113] and deducing linear models for predicting activation enthalpies of organic and organometallic reacting systems.[114]

As expected, ELF disynaptic basins associated with the substituent positions show the most substantial variations in population (≈ *0.1e*), specifically V(C2,O2) and V(C4,O4). Nonetheless, the O-acetyl group exerts a discernible influence on nearby basins, as evidenced by the decrease of approximately *0.1e* in the V(C1,O1) population. While electron populations along the pyran ring maintain near-constant levels, the most relevant changes (± *0.03e*) are observed over V(C1,O), the bonding region featuring the ring-opening process. The relatively low population of V(C1,O), V(C1,O1), V(C2,O2), V(C3,O3), and V(C4,O4) provides insights into the significance attributed to ring opening/contraction and eliminations as these classes of reactions comprise such basins, as detailed in Table 6.

Table 6. Electron population (e) of xylose, 2-O-acetyl-xylose, and 4-O-methyl-D-glucuronic acid at the M06-2X/6-311++G(d,p) level.

ELF Basin[1]	**Xylose**	**2-O-acetyl-xylose**	**4-O-methyl-D-glucuronic acid**
V(C1,O)	1.35	1.38	1.33
V(C1,C2)	2.08	2.08	2.07
V(C2,C3)	2.02	2.01	2.02
V(C3,C4)	2.02	2.02	2.02
V(C4,C5)	2.01	2.01	1.99
V(C5,O)	1.29	1.29	1.29
V(C1,O1)	1.41	1.36	1.42
V(C2,O2)	1.29	1.39	1.29
V(C3,O3)	1.28	1.28	1.29
V(C4,O4)	1.27	1.27	1.32

[1] The labeling of oxygen matches the pattern delineated by the *Ci-Oi* bonding notation.

Both the global and local chemical reactivity indices[51,52,115] leverage electron density as a foundational parameter to extract meaningful chemical information. This physical-observable-based approach streamlines the correlation of theoretical insights with experimental observations, thereby providing depth to the analyses in the context of thermokinetic discussions. The electronic chemical potential, μ, reveals that the O-acetyl functionalized species is the most reactive (- *4.80* eV), whereas the double substituted reactant displays the lowest reactivity (- *4.62* eV). In contrast, xylose's susceptibility to exchanging electron density falls between these two values (i.e., μ = - *4.75* eV). The relatively high global reactivity of 2-O-acetyl-xylose might be indicative of the moderate thermodynamic stability of the functional group since they can be straightforwardly dissociated through acetic acid, as observed in experiments.[27,30]

The striking low values of Fukui's functions f^+, f^-, and f^0 reveal the extremely weak local reactivity of the investigated chemical species and justify the need for FP conditions. Moreover, this suggests the implausibility of the investigated processes being reversible, aligning with their thermodynamically favorable nature. Both the O-acetyl and methoxy functional groups consistently modulate the propensity of the system toward electrophilic attacks near C2 and C4, respectively; in contrast, while the latter significantly increases this probability at O4, the former lowers it in the locality of O2, as evidenced in Figure 3, Panel a. The value of f^+ drops at the C2, C4, O2, and O4 centers, indicating that the substituents lower the propensity to a nucleophilic attack in their vicinity, see Figure 6, Panel b. The C2, C4, and O2 regions are less prone to a neutral (or radical) attack, while the probability notably increases at O4, see Figure 6, Panel c. For xylose, the preeminent reactivity of the pyran-ring oxygen might potentially support the notion that the ring-opening is the fastest reaction, as indicated by the highest values of f^- and f^0 compared with its other centers. Similarly, 4-O-methyl-D-glucuronic acid exhibits peak values for these functions for the methoxy oxygen (O4), possibly justifying the barrier reduction and the relatively high rate observed in one of the processes involving this functional group, namely, the elimination associated with TS-AXPL7. Intriguingly, in the case of 2-O-acetyl-xylose, *all* Fukui's functions are minimized at both C2 and O2, whereas f^- and f^0 are maximized at the C3 and O3 atoms. This signifies that O-acetyl diminishes the centers reactivity at the substituent position, while significantly favors it at the neighboring reacting center, C3. Nonetheless, these observations closely match the thermokinetic findings since the elimination undergone via TS-AXPL3 involving C3 is the reaction with the lowest barrier and highest rate, excluding ring-opening. For functionalized species, *none* of these local functions exhibits a notable peak at the pyran-ring oxygen, which contradicts the results derived from the thermokinetic analysis. Thus, these outcomes fall short of elucidating the thermokinetic observations across all structural motifs consistently.

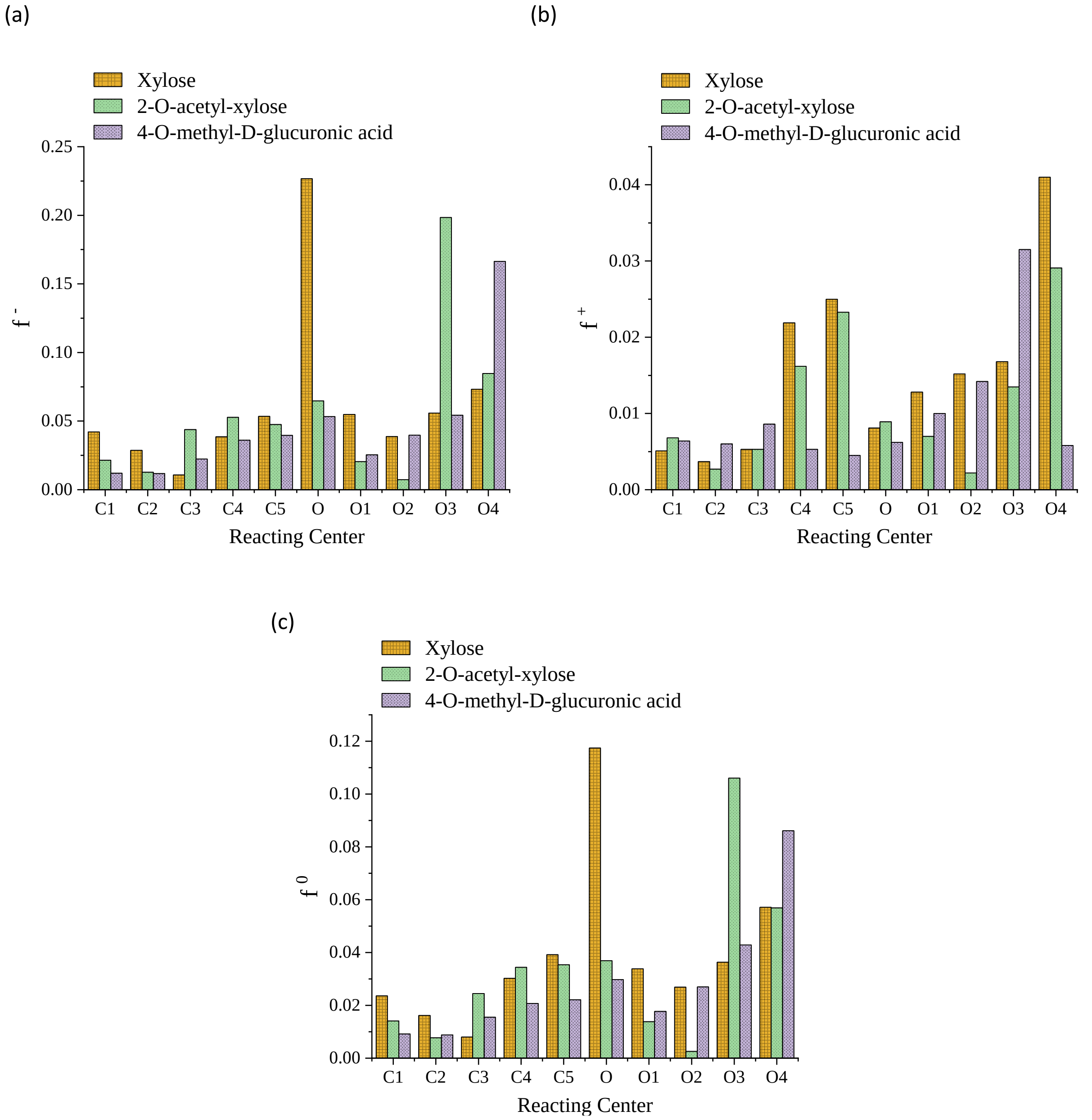

Figure 3. Fukui's functions f^- (Panel a), f^+ (Panel b), and f^0 (Panel c) of reacting centers involved in ring opening/contraction and eliminations undergone by xylose, 2-O-acetyl-xylose, and 4-O-methyl-D-glucuronic acid reactants at the M06-2X/6-311++G(d,p) level. The labeling of centers matches the pattern delineated by the C*i*-O*i* bonding notation.

Conclusions

In this study, we have analyzed the thermodynamic and kinetic effects of functional groups on the pyrolytic depolymerization of β-D-xylopyranose, a pivotal hemicellulose motif. Two distinct moieties, namely, 2-O-acetyl-β-D-xylopyranose and 4-methoxy-5-carboxy-β-D-xylopyranose, have been carefully selected to conduct this investigation as they have been experimentally isolated from various types of hemicellulose plant matter, a biomass main component relatively less studied compared to cellulose. Through state-of-the-art density functional, composite chemistry methods, and transition state theory, we here reported for the first time quite complete thermochemical data for carbohydrates to aid in developing reliable kinetic models. Such a dataset includes activation barrier, standard enthalpy of formation, Gibbs free energy, heat capacities, and rate constant at various temperatures for three initial reaction classes understood to decompose carbohydrates under pyrolysis conditions: ring-opening, ring-contraction, and elimination. The results demonstrated high reliability, as evidenced by the close agreement (i.e., below *0.5* kcal mol^{-1}) between computed and experimental enthalpies of formation upon spin-orbit corrections for pyrolytic products of elimination reactions: water, acetic acid, and methanol. In this vein, the predicted standard enthalpy of formation of β-D-xylopyranose, 4-methoxy-5-carboxy-β-D-xylopyranose, and 2-O-acetyl-β-D-xylopyranose are determined to be *-218.2*, *-263.1*, and *-300.0* kcal/mol, respectively. Across all examined species, the ring-opening barrier felt approximately within *43.8-47.5* kcal mol^{-1}, in contrast to the higher activation enthalpies observed for ring-contraction and elimination, ranging from *61.0* to *81.1* kcal mol^{-1}. Irrespective of the functionalization, the pathway leading to acyclic products was the fastest, featuring a rate constant in the order of *10* s^{-1}, significantly superior to the rate characterizing the other reaction types, which ranged from 10^{-10} and 10^{-4} s^{-1} for the other reaction types. Curiously, the most reactive elementary step is the only thermodynamically unfavorable reaction within the Fast Pyrolysis regime. The thermochemical and kinetic analyses consistently showed that introducing functional groups lowers the barrier by *1.9* to *8.3* kcal mol^{-1}. Consequently, the rate constant increased by *0* to *4* orders of magnitude concerning the unfunctionalized system. However, this catalytic-like effect strongly depends on the relative spatial rearrangements of reacting centers and proved insufficient to effectively bridge the competition between processes, evidencing the significant role of steric effects and regioselectivity. Our study emphasizes the relevance of conformational analysis. This must receive more frequent attention due to the high geometric flexibility exhibited by biomass main components, providing thus the generality needed for forthcoming endeavors. It is quite promising that a straightforward chemical reactivity and bonding analysis offer partial corroboration for the thermokinetic findings. These insights notably simplify the exploration of potential energy surfaces of hemicelluloses pyrolysis by offering to circumvent numerous alternative depolymerization pathways.

Author Contributions

L. A.-H., S. D.: project supervision, conceptualization, data analysis, and manuscript writing; L. A.-H., J. L.: calculations, reaction paths, and characterization. All authors reviewed and commented on the manuscript.

Conflicts of interest

There are no conflicts to declare.

Acknowledgements

The authors acknowledge the European Research Council (ERC) and Science Foundation of Ireland (SFI) for the continuous financial support through Nos. 101002649 and 12/RC/2278_2, respectively. We are also indebted to the Irish Centre for High-End Computing (ICHEC) for the computational resources provision through projects tcche 139–141. In addition, we thank Drs. Bernardo Ballotta, Liam Mannion, and Mark Kelly for significantly enriching this work through insightful discussions.

Author Information

Corresponding Authors

*Leandro Ayarde-Henríquez – School of Physics, Trinity College Dublin, Dublin, Ireland. Advanced Materials and BioEngineering Research Centre, Dublin, Ireland. https://orcid.org/0000–0001–5963–6028. E–mail: leandro.ayarde@tcd.ie
*Stephen Dooley – School of Physics, Trinity College Dublin, Dublin, Ireland. Advanced Materials and BioEngineering Research Centre, Dublin, Ireland. https://orcid.org/0000-0001-9450-8486. E–mail: stephen.dooley@tcd.ie

References

1 M. Brennan Pecha, J. I. M. Arbelaez, M. Garcia-Perez, F. Chejne and P. N. Ciesielski, *Green Chemistry*, 2019, 21, 2868–2898.

2 J. N. Chheda, G. W. Huber and J. A. Dumesic, Liquid-phase catalytic processing of biomass-derived oxygenated hydrocarbons to fuels and chemicals, *Angewandte Chemie - International Edition*, 2007, **46**, 7164–7183.

3 M. K. Ghosh, M. S. Howard, K. Dussan and S. Dooley, Mechanism and theory of d-glucopyranose homogeneous acid catalysis in the aqueous solution phase, *Physical Chemistry Chemical Physics*, 2019, **21**, 17993–18011.

4 S. Wang, G. Dai, H. Yang and Z. Luo, *Prog Energy Combust Sci*, 2017, 62, 33–86.

5 B. Hu, B. Zhang, W. L. Xie, X. Y. Jiang, J. Liu and Q. Lu, Recent Progress in Quantum Chemistry Modeling on the Pyrolysis Mechanisms of Lignocellulosic Biomass, *Energy and Fuels*, 2020, **34**, 10384–10440.

6 K. Dussan, S. Dooley and R. Monaghan, Integrating compositional features in model compounds for a kinetic mechanism of hemicellulose pyrolysis, *Chemical Engineering Journal*, 2017, **328**, 943–961.

7 D. N. S. Hon, Cellulose: a random walk along its historical path, *Cellulose*, 1994, **1**, 1–25.

8 A. G. McDonald and L. A. Donaldson, *Encyclopedia of Materials: Science and Technology*, 2001, 9612–9616.

9 R. T. Olsson, L. Fogelström, M. Martínez-Sanz and M. Henriksson, in *Multifunctional and Nanoreinforced Polymers for Food Packaging*, Elsevier, 2011, pp. 86–107.

10 E. Rudnik, in *Handbook of Biopolymers and Biodegradable Plastics: Properties, Processing and Applications*, Elsevier Inc., 2013, pp. 189–211.

11 O. Benaimeche, N. T. Seghir, Ł. Sadowski and M. Mellas, in *Encyclopedia of Renewable and Sustainable Materials*, Elsevier Ltd., 2020, pp. 649–662.

12 R. A. Hussein and A. A. El-Anssary, in *Herbal Medicine*, ed. P. Builders, IntechOpen, 2019, pp. 11–30.

13 A. J. Yanez, W. Li, R. Mabon and L. J. Broadbelt, A Stochastic Method to Generate Libraries of Structural Representations of Lignin, *Energy and Fuels*, 2016, **30**, 5835–5845.

14 M. Abu-Ghalia and Y. Dahman, in *Lignocellulosic Fibre and Biomass-Based Composite Materials: Processing, Properties and Applications*, Elsevier Inc., 2017, pp. 313–345.

15 C. Chio, M. Sain and W. Qin, Lignin utilization: A review of lignin depolymerization from various aspects, *Renewable and Sustainable Energy Reviews*, 2019, **107**, 232–249.

16 M. K. Ghosh, M. S. Howard, Y. Zhang, K. Djebbi, G. Capriolo, A. Farooq, H. J. Curran and S. Dooley, The combustion kinetics of the lignocellulosic biofuel, ethyl levulinate, *Combust Flame*, 2018, **193**, 157–169.

17 M. S. Mettler, D. G. Vlachos and P. J. Dauenhauer, *Energy Environ Sci*, 2012, 5, 7797–7809.

18 X. Zhou, W. Li, R. Mabon and L. J. Broadbelt, A critical review on hemicellulose pyrolysis, *Energy Technology*, 2017, **5**, 52–79.

19 R. Vinu and L. J. Broadbelt, A mechanistic model of fast pyrolysis of glucose-based carbohydrates to predict bio-oil composition, *Energy Environ Sci*, 2012, **5**, 9808–9826.

20 E. Ranzi, P. E. A. Debiagi and A. Frassoldati, Mathematical Modeling of Fast Biomass Pyrolysis and Bio-Oil Formation. Note I: Kinetic Mechanism of Biomass Pyrolysis, *ACS Sustain Chem Eng*, 2017, **5**, 2867–2881.

21 Z. Dong, Z. Liu, X. Zhang, H. Yang, J. Li, S. Xia, Y. Chen and H. Chen, Pyrolytic characteristics of hemicellulose, cellulose and lignin under CO2 atmosphere, *Fuel*, 2019, **256**, 115890.

22 D. Chen, K. Cen, X. Zhuang, Z. Gan, J. Zhou, Y. Zhang and H. Zhang, Insight into biomass pyrolysis mechanism based on cellulose, hemicellulose, and lignin: Evolution of volatiles and kinetics, elucidation of reaction pathways, and characterization of gas, biochar and bio-oil, *Combust Flame*, 2022, **242**, 112142.

23 K. Dussan, S. Dooley and R. Monaghan, Integrating compositional features in model compounds for a kinetic mechanism of hemicellulose pyrolysis, *Chemical Engineering Journal*, 2017, **328**, 943–961.

24 M. Kelly, M. Fortune, G. Bourque and S. Dooley, Machine learned compact kinetic models for methane combustion, *Combust Flame*, 2023, **253**, 112755–14.

25 P. Capek and J. Alfo, An acetylated galactoglucomannan from Picea abies L. Karst, *Carbohydr Res*, 2002, **337**, 1033–1037.

26 A. Teleman, M. Tenkanen, A. Jacobs and O. Dahlman, Characterization of O-acetyl-(4-O-methylglucurono)xylan isolated from birch and beech, *Carbohydr Res*, 2002, **337**, 373–377.

27 S. Wang, B. Ru, H. Lin and W. Sun, Pyrolysis behaviors of four O-acetyl-preserved hemicelluloses isolated from hardwoods and softwoods, *Fuel*, 2015, **150**, 243–251.

28 K. Shimizu, Kazuma; Hashi, Mieko; Sakurai, Isolation from a Softwood Xylan of Oligosaccharides Containing two 4-O-Methyl-D-Glucuronic Acid Residues, *Carbohydr Res*, 1978, **62**, 117–126.

29 S. Sakamoto, K. Yoshida, S. Sugihara and N. Mitsuda, Development of a new high-throughput method to determine the composition of ten monosaccharides including 4-O-methyl glucuronic acid from plant cell walls using ultra-performance liquid chromatography, *Plant Biotechnology*, 2015, **32**, 55–63.

30 S. Wang, B. Ru, H. Lin and Z. Luo, Degradation mechanism of monosaccharides and xylan under pyrolytic conditions with theoretic modeling on the energy profiles, *Bioresour Technol*, 2013, **143**, 378–383.

31 J. B. Huang, C. Liu, H. Tong, W. M. Li and D. Wu, Theoretical studies on pyrolysis mechanism of O-acetyl-xylopyranose, *Ranliao Huaxue Xuebao/Journal of Fuel Chemistry and Technology*, 2013, **41**, 285–293.

32 D. K. Shen, S. Gu and A. V. Bridgwater, Study on the pyrolytic behaviour of xylan-based hemicellulose using TG-FTIR and Py-GC-FTIR, *J Anal Appl Pyrolysis*, 2010, **87**, 199–206.

33 B. Ru, S. Wang, G. Dai and L. Zhang, Effect of Torrefaction on Biomass Physicochemical Characteristics and the Resulting Pyrolysis Behavior, *Energy and Fuels*, 2015, **29**, 5865–5874.

34 S. Wang, G. Dai, B. Ru, Y. Zhao, X. Wang, J. Zhou, Z. Luo and K. Cen, Effects of torrefaction on hemicellulose structural characteristics and pyrolysis behaviors, *Bioresour Technol*, 2016, **218**, 1106–1114.

35 M. J. Frisch, G. W. Trucks, H. B. Schlegel, G. E. Scuseria, M. A. Robb, J. R. Cheeseman, G. Scalmani, V. Barone, B. Mennucci, G. A. Petersson, H. Nakatsuji, X. Li, M. Caricato, A. V. Marenich, J. Bloino, B. G. Janesko, R. Gomperts, B. Mennucci, H. P. Hratchian, J. V. Ortiz, A. F. Izmaylov, J. L. Sonnenberg, D. Williams-Young, F. Ding, F. Lipparini, J. Goings, B. Peng, A. Petrone, T. Henderson, D. Ranasinhe, V. G. Zakrzewski, J. Gao, N. Rega, G. Zheng, W. Liang, M. Hada, M. Ehara, K. Toyota, R. Fukuda, J. Hasegawa, M. Ishida, T. Nakajima, Y. Honda, O. Kitao, H. Nakai, T. Vreven, K. Throssell, A. Montgomery Jr., J. E. Peralta, F. Ogliaro, M. Bearpark, E. J. J. Heyd, N. Brothers, K. N. Kudin, V. N. Staroverov, T. A. Keith, R. Kobayashi, J. Normand, K. Raghavachari, A. Rendell, J. C. Burant, S. S. Iyengar, J. Tomasi, M. Cossi, J. M. Millam, M. Klene, C. Adamo, J. R. Cammi, W. Ochterski, R. L. Martin, K. Morokuma, Ö. Farkas, J. B. Foresman and D. J. Fox, Gaussian 16, Revision B.01, 2016.

36 Y. Zhao and D. G. Truhlar, The M06 suite of density functionals for main group thermochemistry, thermochemical kinetics, noncovalent interactions, excited states, and transition elements: Two new

functionals and systematic testing of four M06-class functionals and 12 other function, *Theor Chem Acc*, 2008, **120**, 215–241.

37 K. Fukui, A formulation of the reaction coordinate, *J Phys Chem*, 1970, **74**, 4161.

38 T. J. Lee and P. R. Taylor, A Diagnostic for Determining the Quality of Single-Reference Electron Correlation Methods, *Int J Quantum Chem: Quantum Chem Symposium*, 1989, **23**, 199–207.

39 P. Pracht, F. Bohle and S. Grimme, Automated exploration of the low-energy chemical space with fast quantum chemical methods, *Physical Chemistry Chemical Physics*, 2020, **22**, 7169–7192.

40 J. A. Montgomery, M. J. Frisch, J. W. Ochterski and G. A. Petersson, A complete basis set model chemistry. VI. Use of density functional geometries and frequencies, *Journal of Chemical Physics*, 1999, **110**, 2822–2827.

41 J. A. Montgomery, M. J. Frisch, J. W. Ochterski and G. A. Petersson, A complete basis set model chemistry. VII. Use of the minimum population localization method, *Journal of Chemical Physics*, 2000, **112**, 6532–6542.

42 L. A. Curtiss, P. C. Redfern and K. Raghavachari, Gaussian-4 theory, *Journal of Chemical Physics*, 2007, **126**, 1–12.

43 T. Lu and Q. Chen, Shermo: A general code for calculating molecular thermochemistry properties, *Comput Theor Chem*, 2021, **1200**, 113249.

44 R. O. Ramabhadran and K. Raghavachari, Connectivity-Based Hierarchy for theoretical thermochemistry: Assessment using wave function-based methods, *J Phys Chem A*, 2012, **116**, 7531–7537.

45 D. W. Rogers, A. A. Zavitsas and N. Matsunaga, Determination of enthalpies ('Heats') of formation, *WIRES Comput Mol Sci*, 2013, **3**, 21–36.

46 B. Ruscic, R. E. Pinzon, M. L. Morton, G. Von Laszevski, S. J. Bittner, S. G. Nijsure, K. A. Amin, M. Minkoff and A. F. Wagner, Introduction to active thermochemical tables: Several 'Key' enthalpies of formation revisited, *Journal of Physical Chemistry A*, 2004, **108**, 9979–9997.

47 B. Ruscic, R. E. Pinzon, G. Von Laszewski, D. Kodeboyina, A. Burcat, D. Leahy, D. Montoy and A. F. Wagner, Active Thermochemical Tables: Thermochemistry for the 21st century, *J Phys Conf Ser*, 2005, **16**, 561–570.

48 S. Canneaux, F. Bohr and E. Henon, KiSThelP: A program to predict thermodynamic properties and rate constants from quantum chemistry results, *J Comput Chem*, 2014, **35**, 82–93.

49 R. G. Parr, R. A. Donnelly, M. Levy and W. E. Palke, Electronegativity: The density functional viewpoint, *J Chem Phys*, 1978, **68**, 3801–3807.

50 R. G. Parr and W. Yang, Theory of Orientation and Steroselection, *Annu Rev Phys Chem*, 1984, **106**, 4050–4051.

51 P. Geerlings, F. De Proft and W. Langenaeker, Conceptual density functional theory, *Chem Rev*, 2003, **103**, 1793–1873.

52 L. Shubin, Conceptual Density Functional Theory and Some Recent Developments, *Acta Phys. Chim. Sin.*, 2009, **25**, 590–600.

53 F. De, P. W. Ayers and P. Geerlings, in *The Chemical Bond*, eds. G. Frenkin and S. Shaik, Wiley -VCH, Weinheim, 2014, pp. 233–269.

54 F. De Profit, in *Conceptual Density Functional Theory: Towards a New Chemical Reactivity Theory*, ed. S. Liu, WILEY-VCH, Weinheim, 1st edn., 2022, pp. 17–46.

55 A. D. Becke and K. E. Edgecombe, A simple measure of electron localization in atomic and molecular systems, *J Chem Phys*, 1990, **92**, 5397–5403.

56 M. Kohout and A. Silvi, Atomic Shell Structure and Electron Numbers, *Int J Quantum Chem*, 1996, **60**, 875–882.

57 J. Andrés, P. Gonz and V. S. Safont, Unraveling Reaction Mechanisms by Means of Quantum Chemical Topology Analysis, *International Journal of Quantum Chemistry 2014*, 2014, **114**, 1239–1252.

58 P. Fuentealba, E. Chamorro and J. C. Santos, in *Theoretical and Computational Chemistry*, ed. T.-L. A, Elsevier B.V., 1ed edn., 2007, pp. 57–85.

59 A. Savin, R. Nesper, S. Wengert and T. F. Fässler, ELF: The electron localization function, *Angew Chem, Inter Ed Engl*, 1997, **36**, 1808–1832.

60 A. Savin, A. D. Becke, J. Flad, R. Nesper, H. Preuss and H. G. von Schnering, A New Look at Electron Localization, *Angew Chem, Int Ed Engl*, 1991, **30**, 409–412.

61 B. Silvi, The synaptic order: A key concept to understand multicenter bonding, *J Mol Struct*, 2002, **614**, 3–10.

62 A. Savin, B. Silvi and F. Colonna, Topological analysis of the electron localization function applied to delocalized bonds, *Can J Chem*, 1996, **74**, 1088–1096.

63 T. Lu and F. Chen, Multiwfn: A multifunctional wavefunction analyzer, *J Comput Chem*, 2012, **33**, 580–592.

64 B. Hu, Q. Lu, Z. X. Zhang, Y. T. Wu, K. Li, C. Q. Dong and Y. P. Yang, Mechanism insight into the fast pyrolysis of xylose, xylobiose and xylan by combined theoretical and experimental approaches, *Combust Flame*, 2019, **206**, 177–188.

65 L. Radom, W. J. Hehre and J. A. Pople, Molecular Orbital Theory of the Electronic Structure of Organic Compounds. VII. A Systematic Study of Energies, Conformations, and Bond Interactions, *J Amer Chem Soc*, 1971, **93**, 289–300.

66 W. J. Hehre, R. Ditchfield, L. Radom and J. A. Pople, Molecular Orbital Theory of the Electronic Structure of Organic Compounds. V. Molecular Theory of Bond Separation, *J Amer Chem Soc*, 1970, **92**, 4796–4801.

67 R. O. Ramabhadran and K. Raghavachari, Theoretical thermochemistry for organic molecules: Development of the generalized connectivity-based hierarchy, *J Chem Theory Comput*, 2011, **7**, 2094–2103.

68 S. E. Wheeler, K. N. Houk, P. V. R. Schleyer and W. D. Allen, A Hierarchy of homodesmotic reactions for thermochemistry, *J Am Chem Soc*, 2009, **131**, 2547–2560.

69 M. K. Ghosh, M. S. Howard and S. Dooley, Accurate and standard thermochemistry for oxygenated hydrocarbons: A case study of ethyl levulinate, *Proceedings of the Combustion Institute*, 2018, **37**, 337–346.

70 C. E. Moore, *Atomic Energy Levels*, Circular of the National Bureau of Standards, Washington, 1949, vol. I.

71 W. C. Martin, Table of Spin-Orbit Energies for p-Electrons in Neutral Atomic (core)np Configurations, *JOURNAL OF RESEARCH of toe Notional Bureau of Standards - A. Physics and Chemistry*, 1970, **75A**, 109–111.

72 A. Shrivastava, in *Introduction to Plastics Engineering*, Elsevier, 2018, pp. 49–110.

73 D. C. Marinescu and G. M. Marinescu, in *Classical and Quantum Information*, Elsevier, 2012, pp. 221–344.

74 J. P. McCullough, R. E. Pennington and G. Waddington, A Calorimetric Determination of the Vapor Heat Capacity and Gas Imperfection of Water, *J Am Chem Soc*, 1952, **74**, 4439–4442.

75 D. R. Stull, E. F. Westrum and G. C. Sinke, *The Chemical Thermodynamics of Organic Compounds*, Wiley, New York, 1969.

76 M. A. V. Ribeiro Da Silva, M. D. M. C. Ribeiro Da Silva, A. I. M. C. Lobo Ferreira, Q. Shi, B. F. Woodfield and R. N. Goldberg, Thermochemistry of α-D-xylose(cr), *J. Chem. Thermodynamics*, 2013, **58**, 20–28.

77 R. V. Jasra and J. C. Ahluwalia, Enthalpies of Solution, Partial Molal Heat Capacities and Apparent Molal Volumes of Sugars and Polyols in Water, *J Solution Chem*, 1982, **11**, 325–338.

78 F. Kawaizumi, S. Kushida and Y. Miyahara, Determination of the Specific Heat Capacities of Aqueous Solutions of Pentose, *Bull. Chem, Soc. Jpn.*, 1981, **54**, 2282–2285.

79 T. R. Brown, A techno-economic review of thermochemical cellulosic biofuel pathways, *Bioresour Technol*, 2015, **178**, 166–176.

80 C. D. Scown, N. R. Baral, M. Yang, N. Vora and T. Huntington, Technoeconomic analysis for biofuels and bioproducts, *Curr Opin Biotechnol*, 2021, **67**, 58–64.

81 R. Mahmud, S. M. Moni, K. High and M. Carbajales-Dale, Integration of techno-economic analysis and life cycle assessment for sustainable process design – A review, *J Clean Prod*, 2021, **317**, 128247.

82 J. C. Quinn and R. Davis, The potentials and challenges of algae based biofuels: A review of the techno-economic, life cycle, and resource assessment modeling, *Bioresour Technol*, 2015, **184**, 444–452.

83 M. Patel, X. Zhang and A. Kumar, Techno-economic and life cycle assessment on lignocellulosic biomass thermochemical conversion technologies: A review, *Renewable and Sustainable Energy Reviews*, 2016, **53**, 1486–1499.

84 R. Davis, L. Tao, E. C. D. Tan, M. J. Biddy, G. T. Beckham, C. Scarlata, J. Jacobson, K. Cafferty, J. Ross, J. Lukas, D. Knorr and P. Schoen, *Process Design and Economics for the Conversion of Lignocellulosic Biomass to Hydrocarbons: Dilute-Acid and Enzymatic Deconstruction of Biomass to Sugars and Biological Conversion of Sugars to Hydrocarbons*, 2013.

85 I. Obernberger, T. Brunner and G. Bärnthaler, Chemical properties of solid biofuels-significance and impact, *Biomass Bioenergy*, 2006, **30**, 973–982.

86 M. H. M. Yasin, M. A. Ali, R. Mamat, A. F. Yusop and M. H. Ali, in *Second and Third Generation of Feedstocks: The Evolution of Biofuels*, Elsevier, 2019, pp. 291–320.

87 P. Hanggi, H. Grabert, G. L. Ingold and U. Weiss, Quantum theory of activated events in presence of long-time memory, *Phys Rev Lett*, 1985, **55**, 761–764.

88 M. J. Gillan, Quantum-classical crossover of the transition rate in the damped double well, *Journal of Physics C: Solid State Physics*, 1987, **20**, 3621–3641.

89 R. J. Gillespie and R. S. Nyholm, A simple electrostatic theory: The arrangement of electron pairs in valency shells, *Q Rev Chem Soc*, 1957, **11**, 339–380.

90 X. Krokidis, S. Noury and B. Silvi, Characterization of elementary chemical processes by catastrophe theory, *J Phys Chem A*, 1997, **101**, 7277–7282.

91 L. Ayarde-Henríquez, C. Guerra, M. Duque-Noreña and E. Chamorro, Revisiting the bonding evolution theory: a fresh perspective on the ammonia pyramidal inversion and bond dissociations in ethane and borazane, *Phys Chem Chem Phys*, 2023, **25**, 27394–27408.

92 I. Viciano, P. González-Navarrete, J. Andrés and S. Martí, Joint Use of bonding evolution theory and QM/MM hybrid method for understanding the hydrogen abstraction mechanism via cytochrome P450 aromatase, *J Chem Theory Comput*, 2015, **11**, 1470–1480.

93 A. S. Nizovtsev, Activation of C-H bond in methane by Pd atom from the bonding evolution theory perspective, *J Comput Chem*, 2013, **34**, 1917–1924.

94 O. Matthies, Y. Grin and M. Kohout, Absent Diamond-to-β-Sn Phase Transition for Carbon: Quantum Chemical Topology Approach, *Chemistry Select*, 2017, **2**, 7659–7669.

95 V. Polo, J. Andrés, S. Berski, L. R. Domingo and B. Silvi, Understanding reaction mechanisms in organic chemistry from catastrophe theory applied to the electron localization function topology, *J Phys Chem A*, 2008, **112**, 7128–7136.

96 P. González-Navarrete, L. R. Domingo, J. Andres, S. Berski and B. Silvi, Electronic fluxes during diels-alder reactions involving 1,2-benzoquinones: Mechanistic insights from the analysis of electron localization function and catastrophe theory, *J Comput Chem*, 2012, **33**, 2400–2411.

97 A. I. Adjieufack, V. Liégeois, I. N. Mboumbouo, M. J. Ketcha and B. Champagne, Intramolecular [3 + 2] Cycloaddition Reactions of Unsaturated Nitrile Oxides. A Study from the Perspective of Bond Evolution Theory (BET), *J Phys Chem A*, 2018, **122**, 7472–7481.

98 M. Ríos-Gutiérrez, P. Pérez and L. R. Domingo, A bonding evolution theory study of the mechanism of [3+2] cycloaddition reactions of nitrones with electron-deficient ethylenes, *RSC Adv*, 2015, **5**, 58464–58477.

99 P. Merino, T. Tejero, I. Delso and R. Matute, New mechanistic interpretations for nitrone reactivity, *Org Biomol Chem*, 2017, **15**, 3364–3375.

100 A. I. Adjieufack, I. M. Ndassa, I. Patouossa, J. K. Mbadcam, V. S. Safont, M. Oliva and J. Andrés, On the outside looking in: rethinking the molecular mechanism of 1,3- dipolar cycloadditions from the perspective of bonding evolution theory. The reaction between cyclic nitrones and ethyl acrylate, *Phys Chem Chem Phys*, 2017, **19**, 18288–18302.

101 L. Ayarde-Henríquez, C. Guerra, M. Duque-Noreña, E. Rincón, P. Pérez and E. Chamorro, On the Notation of Catastrophes in the Framework of Bonding Evolution Theory: the Case of Normal and Inverse Electron Demand Diels-Alder Reactions, *Chem Phys Chem*, 2022, **23**, e202200343.

102 L. Ayarde-Henríquez, C. Guerra, M. Duque-Noreña, E. Rincón, P. Pérez and E. Chamorro, Are There Only Fold Catastrophes in the Diels–Alder Reaction Between Ethylene and 1,3-Butadiene?, *J Phys Chem A*, 2021, **125**, 5152–5165.

103 E. Chamorro, C. Guerra, L. Ayarde-Henríquez, M. Duque-Noreña, P. Pérez and E. Rincón, in *Chemical Reactivity: Theories and Principles*, eds. S. Kayas, L. von Szentpály, G. Serdaroglu and L. Guo, Elsevier, 2023, vol. 1, pp. 465–481.

104 S. Berski and L. Z. Ciunik, The mechanism of the formation of the hemiaminal and Schiff base from the benzaldehyde and triazole studied by means of the topological analysis of electron localisation function and catastrophe theory, *Mol Phys*, 2015, **113**, 765–781.

105 A. Ćmikiewicz, A. J. Gordon and S. Berski, Characterisation of the reaction mechanism between ammonia and formaldehyde from the topological analysis of ELF and catastrophe theory perspective, *Struct Chem*, 2018, **29**, 243–255.

106 C. Guerra, L. Ayarde-Henríquez, E. Chamorro and A. Ensuncho, Uncovering Triradicaloid Structures in S1 Benzene Photochemistry**, *Chem Photo Chem*, 2023, **7**, e202200263.

107 C. Guerra, L. Ayarde-Henríquez, M. Duque-Noreña and E. Chamorro, Photochemically induced 1,3-butadiene ring-closure from the topological analysis of the electron localization function viewpoint, *Chem Phys Chem*, 2022, **23**, 202200217.

108 C. Guerra, L. Ayarde-Henríquez, M. Duque-Noreña and E. Chamorro, On Electron Pair Rearrangements in Photochemical Reactions: 1,3-Cyclohexadiene Ring Opening, *J Phys Chem A*, 2021, **126**, 395–405.

109 C. Guerra, L. Ayarde-Henríquez, M. Duque-Noreña and E. Chamorro, Unraveling the Bonding Nature Along the Photochemically Activated Paterno-Büchi Reaction Mechanism, *Chem Phys Chem*, 2021, **22**, 2342–2351.

110 C. Guerra, L. Ayarde-Henríquez, Y. A. Rodríguez-Núñez, A. Ensuncho and E. Chamorro, Elucidating the N−N and C−N Bond-breaking Mechanism in the Photoinduced Formation of Nitrile Imine, *Chem Phys Chem*, 2023, **24**, e202200867.

111 C. Guerra, L. Ayarde-Henríquez, M. Duque-Noreña, C. Cárdenas, P. Pérez and E. Chamorro, On the nature of bonding in the photochemical addition of two ethylenes: C-C bond formation in the excited state?, *Phys Chem Chem Phys*, 2021, **23**, 20598–20606.

112 C. Guerra, L. Ayarde-Henríquez, Y. A. Rodriguez-Nuñez, E. Chamorro and A. E. Ensuncho, Mechanistic insights into benzyne formation via 1,2-di-iodobenzene photolysis, *New Journal of Chemistry*, 2023, **47**, 21270–21275.

113 J. Contreras-García, A. Martín Pendás, J. M. Recio and B. Silvi, Computation of local and global properties of the electron localization function topology in crystals, *J Chem Theory Comput*, 2009, **5**, 164–173.

114 L. Ayarde-Henríquez, C. Guerra, M. Duque-Noreña and E. Chamorro, A simple topology-based model for predicting the activation barriers of reactive processes at 0 K, *Phys Chem Chem Phys*, 2023, **25**, 14274–14284.

115 R. K. Roy and S. Saha, in *Annual Reports on the Progress of Chemistry - Section C*, 2010, vol. 106, pp. 118–162.